Fermilab FERMILAB-THESIS-1994-16

Measurement of the W Boson Mass in Proton-Antiproton Collisions at $\sqrt{s} = 1.8\,TeV$

By

Qiang Zhu

A dissertation submitted in partial fulfillment
of the requirements for the degree of
Doctor of Philosophy

The Department of Physics
New York University

April, 1994

Approved

Prof. John Sculli

To Xian, Rebecca and my parents

ACKNOWLEDGEMENTS

I would first like to express my sincere thanks to my advisor, John Sculli, for his guidance during the past six years. It is a pleasure to work with John. I found that I could always count on John's advice whenever I had doubts in either my professional or personal life. His insight in physics and years of experience make his advice invaluable to a student. I could not possibly count the many hours John spends solving problems with his students. I learned a lot of physics and experimental technique from him. There are times in the past six years when things could have been very difficult if it were not for John's help. Although I couldn't possibly list them all, I can summarize it: John is an excellent physicist and a true mentor. He takes the role of advisor as a serious mission. He does not compromise, no matter how much time or hard work is involved. I would also like to thank John for patiently correcting my writing. I learned to write better after reading John's modifications.

I would also like to thank Peter Nemethy. Discussion with Peter is always fruitful. I always received constructive criticism and good advice from Peter.

I would like to express my thanks to the whole W mass group. Special thanks go to Raymond Brock, of Michigan State University, for his efforts in bringing the W mass analysis together and to Marcel Demarteau, of Fermilab, for much help and many useful discussions.

I found my experience working on the DØ experiment a very positive one. The thesis work would not have been possible without the successful data taking of the first DØ collider run. I thank our spokesperson, Paul Grannis, for his strong leadership.

I would like to thank all my colleagues on the DØ experiment, and the support personnel at Fermilab as well. Their many hours of hard work made the experiment possible. I am especially grateful to my colleagues at NYU– James Kourlas, Allen

Mincer, Jonathan Kotcher, Kathy Streets and Jie Yang for their support and help.

I had many profitable discussions with Hiro Aihara of Lawrence Berkeley Laboratory and Geary Eppley of Rice. Geary provided last minute assistance on numerous occasions to help me meet deadlines, for which I am grateful. I thank also Michael Rijssenbeek who first invited me to work on the W mass fitting.

Very special thanks go to my wife, Xian Wang, and my daughter, Rebecca Xi Zhu. Xian assumed almost all the hard work in caring for our baby. I would not have been able to spend the many hours I did on my thesis work without Xian's strong encouragement and support. My little girl, XiXi, one and a half years old now, has given us lots of joy. She constantly reminds me of how wonderful life is even when I'm tired and sometimes depressed. I would also like to thank Xian's parents for their support during the past few years. Finally, I would like to thank my parents. They first aroused my interest in science, and have always supported me in my career.

Contents

1 Introduction **1**

2 Standard Model and the W Mass **4**

2.1 Standard Model 4

2.2 Hadronic $W^{\pm}$ Production 7

2.2.1 W^{+} Differential Cross Section 8

2.3 W Mass Measurement Technique 10

3 The DØ Detector **13**

3.1 Central Tracking(CD) 14

3.1.1 Vertex Detector(VTX) 14

3.1.2 Transition Radiation Detector(TRD) 15

3.1.3 Central Drift Chambers(CDC) 15

3.1.4 Forward and Backward Drift Chambers(FDC) 15

3.1.5 Read Out Electronics 16

3.2 Calorimeter 16

3.2.1 Central Calorimeter 17

3.2.2 End Calorimeters 18

3.2.3 Intercryostat Detectors 19

3.2.4 Calorimeter Readout Electronics 19

3.3 Hardware and Software Triggers 21
3.3.1 Hardware Trigger : Level 0 and Level 1 Trigger 21
3.3.2 Software Trigger : Level 2 trigger 22
3.4 Offline Data Reconstruction 22

4 Trigger and Offline Event Selection 24
4.1 Data Collection 24
4.2 Online Triggers 26
4.3 Offline Event Selection 26
4.3.1 Electron Identification 27
4.3.2 Missing P_T Measurement 29
4.3.3 Selection Criteria 30
4.4 Background 34
4.4.1 QCD background 34
4.4.2 $W \longrightarrow \tau\nu;\ \tau \longrightarrow e\overline{\nu_e}\nu_\tau$ Background 36
4.4.3 $Z \longrightarrow ee$ Background 37

5 Detector Energy Scale Calibration 38
5.1 Energy Scale Carryover From Test Beam 38
5.2 Calorimeter Azimuthal Uniformity 39
5.2.1 Energy Flow Method and Error Analysis 40
5.2.2 Simple Monte Carlo Simulation 43
5.2.3 Using All EM Triggers From Normal Data Taking 44
5.2.4 Data Set With Special EM Triggers 47
5.3 Z Mass Measurement And Energy Scale 50
5.3.1 Z Mass Fitting Method I 50
5.3.2 Z Mass Fitting Method II 54

6 Monte Carlo Simulation Of W Events **57**

6.1 W^+ Production 58

6.2 Fast Monte Carlo Detector Simulation 63

6.2.1 Electron Energy Resolution 64

6.2.2 Hadronic Response Of P_T^W Recoil 67

6.2.3 Trigger And $u_{||}$ Efficiencies 69

6.2.4 $W \longrightarrow \tau\nu \longrightarrow e\nu\nu$ Decay Effect 74

6.3 Comparisons Between Fast MC And Data, And Mass Fitting Procedure 74

7 Systematic And Energy Scale Uncertainties **78**

7.1 Systematic Uncertainties 78

7.1.1 Trigger Efficiencies 79

7.1.2 Electron Energy Resolution 79

7.1.3 Neutrino P_T Scale And Resolution 79

7.1.4 Energy Underlying An Electron 81

7.1.5 Hadronic To EM Scale 82

7.1.6 QCD Background 82

7.1.7 Structure Functions 82

7.1.8 Uncertainty On The W Width 83

7.1.9 Fitting Error 83

7.1.10 Summary 83

7.2 Uncertainty On EM Energy Scale 83

8 Results **87**

8.1 W Mass From $W \longrightarrow e\nu$ Decay 87

8.2 Consistency Checks 88

8.2.1 Vary Fitting Window 88

8.2.2 Select Single Vertex W Events: 88

8.2.3 Vary The Electron Selection Cuts: 88

9 Conclusions **90**

9.0.4 Method 91

9.0.5 The World Average W Mass 93

9.1 Constraints On Standard Model Parameters 95

9.2 Prospects for Improving Upon the Current Measurements 95

List of Figures

2.1 The correlation between the W mass and the top quark mass. The curves, from top to bottom, correspond to Higgs masses of 60, 100, 250, 600, and 1000 GeV. The upper and lower horizontal lines indicate a $\pm 50 MeV$ measurement of the W mass about a central mass of 80.22 GeV. 6

2.2 The subprocess $u\overline{d} \longrightarrow W^+ \longrightarrow e^+\nu_e$. 9

3.1 The DØ Detector 14

3.2 Calorimeter 17

3.3 Calorimeter η coverage 18

4.1 Run 1(a) Tevatron and DØ Performance. 25

4.2 Distributions in (a) electron transverse momentum and (b) Neutrino transverse momentum. 32

4.3 Distributions in (a) W transverse momentum and (b) W transverse mass. 32

4.4 Comparison of the measured transverse mass distributions with and without the single vertex requirement. In (b) the areas of the distributions are normalized to one. 34

4.5 The distribution in missing P_T of the QCD background (histogram) with W events (data points with error bars) superimposed. The usual requirements on missing P_T and P_T^W are not imposed on the W events. See text for a discussion of the normalization. 35
4.6 Monte Carlo generated transverse mass spectra for W's decaying directly to an electron (signal) and through tau decay (background). (a) linear vertical scale. (b) logarithmic vertical scale. 36

5.1 Differential P_T spectrum of EM clusters observed with special purpose trigger (a) linear vertical scale. (b) logarithmic vertical scale. 42
5.2 MC study. Comparison of input calibration constants to values extracted using the three methods described in text. 45
5.3 Calibration constants used as input in MC study. 45
5.4 Scatter plots of the calibration constants extracted vs the MC input values. (a) Values obtained by *Method I* vs MC inputs. (b) Values obtained by *Method II* vs MC inputs. 46
5.5 Scatter plots of the calibration constants extracted by *Method III* vs the MC input values. 46
5.6 (a) Relative calibration constants for the DØ central calorimeter modules as a function of module ϕ index. (b) The distribution of the calibration constants. 48
5.7 Transverse mass distributions. All distributions are normalized to unity area. (a) no correction; (b) electron energy and missing P_T are corrected by the calibration constants. 51
5.8 Transverse mass distributions. All distributions are normalized to unity area. (a) no correction; (b) electron energy and missing P_T are corrected by the calibration constants. 52

5.9 Transverse mass distributions. All distributions are normalized to unity area. (a) no correction; (b) electron energy and missing P_T are corrected by the calibration constants. 53

5.10 (a) The dielectron invariant mass spectrum compared to theory at the best fit value of the Z mass (b) The negative of the logarithm of the likelihood function (after moving minimum to zero) as a function of the input Z mass. 55

6.1 Valence and sea quark configurations for W^+ production. The light arrows indicate the momentum directions of quarks and antiquarks. The dense arrows indicate the helicities of the quarks and antiquarks. Note the contributions from processes: $qg \longrightarrow W^+q'$ and $\overline{q}g \longrightarrow W^+\overline{q'}$ can be included as part of the contributions to processes (ii) to (v). 60

6.2 The differential cross section for W^+ production as a function of the transverse momentum P_T and pseudorapidity y. 61

6.3 Rapidity distribution of the W^+ boson. Round symbols give the total differential cross section. Triangles give the contribution from valence-valence and valence-sea quarks. Squares give the contribution from sea-sea quarks. 62

6.4 u and d quark structure functions. 62

6.5 The transverse momentum distribution of the W^+. 63

6.6 Distribution in instantaneous luminosity at which W events were acquired. 67

6.7 The P_T^Z obtained from the two electrons minus the P_T^Z calculated from the recoil, projected along the bisector of the angle between the two electron P_T's. Δ vs $\vec{P}_T^{ee} \cdot \hat{\eta}$. (See text for the definition of Δ.) . 70

6.8 Vector diagram showing the projections of the ee and recoil measurements of P_T^Z onto the bi-sector of the angle between the two electron P_T's. 70
6.9 Electron trigger turn-on curves. (a) Turn-on curve measured without z vertex information. (b) Turn-on curve with z vertex measured by Level 0 trigger(called Slow Z vertex). 72
6.10 Missing P_T trigger turn-on curves. Solid line: Turn-on curve measured without z vertex information. Dotted line: Turn-on curve with z vertex measured by Level 0. 72
6.11 $u_{||}$ is the projection of the momentum recoiling against the W along the electron direction (in the transverse plain). 73
6.12 (a) $u_{||}$ vs P_T^W without $u_{||}$ efficiency in the Monte Carlo. (b) $u_{||}$ vs P_T^W with $u_{||}$ efficiency in the Monte Carlo. 73
6.13 Transverse mass spectrum compared to Monte Carlo simulation. The chi-squared was calculated by comparing data and Monte Carlo in 200 MeV bins in transverse mass between 60 GeV and 90 GeV. 76
6.14 Spectrum in P_T^W compared to the Monte Carlo simulation. 76
6.15 The overlap of Monte Carlo simulation(curve) onto data distribution (dots with error bars). (a) Electron P_T. (b) neutrino P_T. 77
6.16 The overlap of Monte Carlo simulation(curve) onto data distribution (dots with error bars). (a) $u_\perp$. (b) $u_{||}$. 77

7.1 A typical W event in the transverse plane: solid lines indicate the measured quantities. See text for the meaning of each item. 80
7.2 Di-electron invariant mass spectrum for J/ψ signal. 86
7.3 Measured Z invariant mass as a function of the f-factor with fitted curve. 86

9.1 The correlation between the W mass and the top quark mass. Various curves from top to bottom correspondent to Higgs masses M_H =60, 100, 250, 600, and 1000 GeV respectively. The middle horizontal line indicates the world average value of the W mass. The upper and lower horizontal lines indicate the one sigma error on the world average. 96

List of Tables

4.1 W event selection cuts 31

4.2 Number of W, Z events in different detector regions 33

5.1 Energy scale corrections 39

5.2 Division of three different regions according to the gain of modules. . 49

5.3 Fits to the W mass for electrons detected in high, medium, and low gain calorimeter modules. 50

6.1 Comparison of the sampling constants $\mathcal{S}$ and $\mathcal{S}'$ in the electron energy resolution (Monte Carlo). 66

6.2 Comparison of the sampling constants $\mathcal{S}$ and $\mathcal{S}'$ in the electron energy resolution (test beam data). The comparison is made for two choices of the sampling fractions. See text for reference. 66

7.1 Systematic uncertainties on the W mass measurement(DØ Preliminary) 84

9.1 A summary of all W mass measurements (unit in GeV). 90

Chapter 1

Introduction

The impressive success of the $SU(3)_c \times SU(2)_L \times U(1)$ gauge theory of strong and electroweak interactions has earned it the title "Standard Model". It has become the standard against which new experimental findings and theories are tested. It accommodates all the present measurements within one or two standard deviations. The discovery of the $W^{\pm}$ and Z^o bosons with the masses, production cross sections, and decay properties predicted by the theory has been its crowning achievement. The Z^o boson mass has been measured very accurately in the Large Electron Positron (LEP) accelerator at the European Nuclear Research Center (CERN). The measured mass is:

$$M_{z^0} = 91.187 \pm 0.007\, GeV[1] \tag{1.1}$$

A precision measurement of the $W^{\pm}$ boson mass is needed.

The top quark is predicted by the Standard Model, but has yet to be observed. A precision measurement of the $W^{\pm}$ mass when combined with existing measurements would result in a very tight constraint on the top quark mass:

$$\Delta(M_w) = 50\, MeV \longrightarrow \Delta(M_{top}) = 9\, GeV[2,\ 40] \tag{1.2}$$

Alternatively, a precise measurement of the W mass and a determination of the

top mass to 10 GeV/c^2 would severely constrain the theory and give information on the Higgs mass.

Although the Standard Model has been very successful so far, it has its own shortcomings. The $SU(2)_L \times U(1)$ electroweak sector has a minium of seventeen independent masses and couplings and its symmetry breaking is based on the trivial free field ($\lambda\Phi^4$) theory. So there is reason for anticipating new physics. It will be interesting to see if the Standard Model holds up under improved electroweak measurements and the measurement of the top quark mass. Any deviation could be a hint of new physics.

These ideas were realized a long time ago [9, 14]. However, it is difficult to measure the W mass with precision, largely because of its production and decay properties.

The W is very heavy and its production cross section very small. Averaging existing measurements, its mass is

$$M_w = 80.22 \pm 0.26\, GeV\ [11,\ 12,\ 15], \tag{1.3}$$

and its production cross section and branching fraction to $e + \nu$ are consistent with expectations:

$$\sigma(P\overline{P} \longrightarrow W^{\pm}X) = 18.6\, nb[3,\ 4] \tag{1.4}$$

$$\frac{,\,(W^+ \longrightarrow e^+\nu_e)}{,\,(W^+)} = 10.5 \pm 0.9\ \%\ [11,\ 12,\ 15]. \tag{1.5}$$

Right now, hadron colliders are the only place to generate $W^{\pm}$ bosons. The Tevatron, at the Fermi National Accelerator Laboratory (FNAL), is the world's highest energy and luminosity hadron collider. It is the ideal place to measure the W boson mass. Two large general purpose detectors have been built and can be used for this measurement. The DØ Detector is one of those detectors.

The determination of the W mass from a study of the decays $W^+ \longrightarrow e^+\nu_e$ and $W^- \longrightarrow e^-\bar{\nu_e}$ will be presented in this thesis.

It is organized as follows. In chapter 2, the Standard Model is described along with its predictions for the W's mass and other properties. The theoretical basis for the W mass measurement is discussed. Chapter 3 describes the DØ Detector; chapter 4, the data taking and W/Z event selection . Chapter 5 deals with detector calibration and energy scale, important to a precision determination of the W mass. In chapter 6, the Monte Carlo technique for simulating W events is given. The physics event generator and the detector simulation are described in detail, as well as the procedure for fitting the W and Z masses. Chapter 7 is devoted to the study of systematic uncertainties. Systematic and scale errors dominate the uncertainty in the W mass measurement. Chapter 8 gives the measurement. Chapter 9 describes the implication of this measurement for the Standard Model and looks into the prospects for high precision measurements in the future.

Chapter 2

Standard Model and the W Mass

2.1 Standard Model

The $SU(3)_c \times SU(2)_L \times U(1)$ gauge theory of strong and electroweak interactions is normally referred to as the Standard Model(SM). It earns its title by providing a good theoretical explanation of an enormous amount of experimental data. It also has been the basis for quite a few important predictions. Using the standard model, the existence and properties of the gluon, and the $W^{\pm}$ and Z^0 bosons were predicted.

The $\{8\}$ dimensional representation of the $SU(3)_{colour}$ gauge theory, Quantum Chromodynamics(QCD), provides a mechanism for binding quarks together into hadrons and also describes the dynamics of the strong interaction.

The $SU(2)_L \times U(1)$ electroweak gauge model with spontaneous symmetry breaking[5, 6, 7] unifies the weak interactions of the $W^{\pm}$ and Z^0 bosons with the electromagnetic interactions. Here the Higgs Mechanism is introduced to give mass to the $W^{\pm}$ and Z^0 bosons and the fermions. The effective single boson exchange

Lagrangian has the form:

$$L_{eff} = \frac{\frac{1}{2}e^2(J^{\mu}_{em})^2}{q^2} + \frac{\frac{1}{2}g^2 J^{+\mu}_L J^-_{L\mu}}{q^2 - M^2_W} + \frac{\frac{1}{2}g^2_Z(J^{\mu}_Z)^2}{q^2 - M^2_Z} \tag{2.1}$$

where J_{em} is the electromagnetic current, $J^{\pm}_L$ are the charged currents, and J_Z is the neutral current. It is customary to introduce a parameter, ρ, which measures the relative strengths of the neutral and charged currents:

$$\rho = (\frac{g^2_Z}{M^2_Z})/(\frac{g^2}{M^2_W}) \tag{2.2}$$

Simple relations exist among the basic parameters.

$$g = \frac{e}{\sin\theta_W} \tag{2.3}$$

$$g' = \frac{e}{\cos\theta_W} \tag{2.4}$$

$$g_Z = \frac{e}{\sin\theta_W cos\theta_W} \tag{2.5}$$

where θ_W is the weak mixing angle. For a given θ_W, all gauge couplings are determined by the electric charge e. At the tree level, the W mass and the Z mass are[9]:

$$M_W = \frac{A}{\sin\theta_W} \tag{2.6}$$

$$M_Z = \frac{A}{\sin\theta_W \cos\theta_W} \tag{2.7}$$

where $\alpha = e^2/4\pi$, $\sin^2\theta_W = 1 - M^2_W/M^2_Z$, and

$$A = (\frac{\pi\alpha}{\sqrt{2}G_F})^{1/2}. \tag{2.8}$$

With A determined from μ and β decay experiments and $\sin^2\theta_W$ obtained from neutrino scattering experiments,

$$A = 37.2810 \pm 0.0003\, GeV^{-1} \tag{2.9}$$

$$\sin^2\theta_W = 0.23 \pm 0.01 \ , \tag{2.10}$$

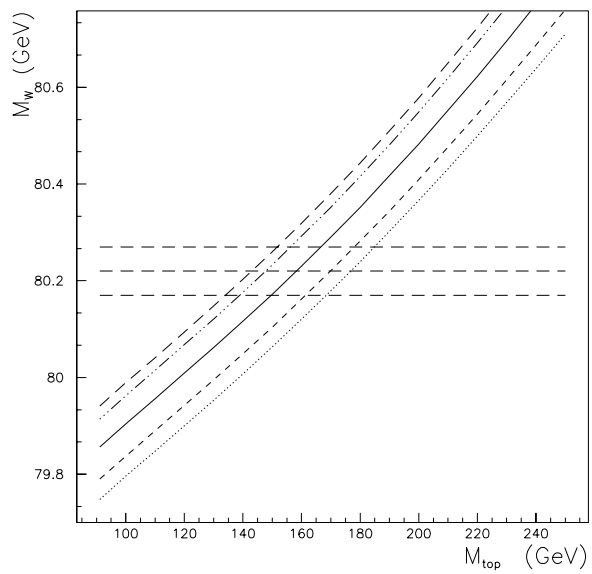

Figure 2.1: The correlation between the W mass and the top quark mass. The curves, from top to bottom, correspond to Higgs masses of 60, 100, 250, 600, and 1000 GeV. The upper and lower horizontal lines indicate a $\pm 50 MeV$ measurement of the W mass about a central mass of 80.22 GeV.

the predicted W mass is

$$M_W = 77.7 \pm 1.7\, GeV\,, \tag{2.11}$$

in disagreement with experimental measurements[11, 12]. This discrepancy results from the failure to include higher order (radiative) corrections to the W mass[9]. One important higher-order effect is the polarization of the vacuum through the creation of virtual fermion-antifermion pairs by the photon. This leads to a modification of the value of α and changes the W and Z masses through Eqs.2.6-2.8. The parameter A should be evaluated with $\alpha(M_Z^2) \simeq 1/128$, not $1/137$ (the low-energy value).

Loop insertions in the W and Z propagators shift their masses. A heavy top quark can lead to a substantial correction of the lowest order result. The top quark contributes to the W and Z self-energy diagrams. They lead to a modification of

Eq. 2.7,

$$M_Z = \frac{A}{\rho \sin\theta_W \cos\theta_W} \tag{2.12}$$

where $\rho \simeq 1 + \frac{3G_F M_t^2}{8\pi^2\sqrt{2}}$. M_t is the top quark mass. We see that the correction depends quadratically on the top quark mass[42].

The Higgs boson also contributes to the W and Z self-energies, leading to an additional term[42]:

$$\Delta\rho = -\frac{3}{8\pi\cos^2\theta_W} ln \frac{M_H}{M_W} \tag{2.13}$$

where M_H is the Higgs mass. We see that the corrections depend strongly on the top quark mass and weakly on the Higgs mass. We can use these dependences to predict the top quark mass when we have accurate W and Z mass measurements. Fig. 2.1 shows the constraint on the top quark mass when we measure the W mass to 50 MeV, which is very likely the ultimate accuracy achievable at hadron colliders.

After the top quark is discovered and its mass measured to some accuracy, e.g. 5 GeV, the W, Z and top quark masses may be combined to obtain information on the Higgs mass.

2.2 Hadronic $W^{\pm}$ Production

$W^{\pm}$ bosons are produced in the hadron collider by the reaction

$$p + \overline{p} \longrightarrow W^{\pm} + X. \tag{2.14}$$

At the quark level:

$$q\overline{q}' \longrightarrow W^{\pm} \tag{2.15}$$

$$\overline{q}g \longrightarrow W^{\pm}\overline{q}\prime \tag{2.16}$$

$$qg \longrightarrow W^{\pm}q\prime \tag{2.17}$$

$$q\overline{q}' \longrightarrow W^{\pm}g \tag{2.18}$$

where q and $\overline{q}'$ can be valence quarks or sea quarks from the p and $\overline{p}$. At the energy of the Tevatron, $\sqrt{s} = 1.8\ TeV$, the sea–valence quark combination gives the biggest contribution to the cross section[3].

The W's have both hadronic and leptonic decay modes. The hadronic decay of the W, e.g., $W \rightarrow u + \bar{d}$, results in two jets in the final state. The rate is small and overwhelmed by dijets produced through ordinary QCD processes. The leptonic decays, on the other hand, are largely free of background. The mass is measured through the leptonic decays of the W. The common leptonic decay channels are:

$$W^+ \longrightarrow e^+\nu_e, \tag{2.19}$$

$$W^- \longrightarrow e^-\overline{\nu_e} \tag{2.20}$$

$$W^+ \longrightarrow \mu^+\nu_\mu \tag{2.21}$$

$$W^- \longrightarrow \mu^-\overline{\nu_\mu} \tag{2.22}$$

We will focus on the electronic decay modes of the W, since these were used to make the W mass measurement reported in this thesis.

2.2.1 W^+ Differential Cross Section

It is illustrative to look at one of the typical subprocesses for $W^\pm$ boson production and decay.

In the subprocess:

$$u\overline{d} \longrightarrow W^+ \longrightarrow e^+\nu_e \tag{2.23}$$

with momenta labeled as in Fig. 2.2, the matrix element is

$$M = \frac{G_F}{\sqrt{2}} M_W^2 V_{ud} \frac{\overline{v}(\overline{d})\gamma_\alpha(1-\gamma_5)u(u)\overline{u}(\nu)\gamma_\alpha(1-\gamma_5)v(e^+)}{\hat{s} - M_W^2 + iM_{W,\,W}} \tag{2.24}$$

where $\hat{s} = (u + \overline{d})^2$ is the square of the center-of-mass energy, and we use standard notation for the Dirac spinors.

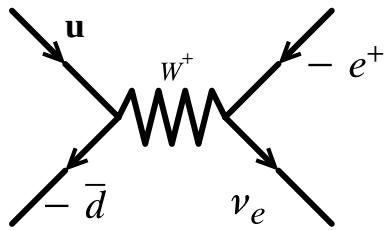

Figure 2.2: The subprocess $u\bar{d} \longrightarrow W^+ \longrightarrow e^+\nu_e$.

The spin-averaged differential cross section is:

$$\frac{d\hat{\sigma}}{d\cos\hat{\theta}} = \frac{|V_{ud}|^2}{\pi\hat{s}^2}(\frac{G_F M_W^2}{\sqrt{2}})^2 \frac{\hat{s}(1+cos\hat{\theta})^2}{(\hat{s}-M_W^2)^2+(,_W M_W)^2} \tag{2.25}$$

where θ is the angle between the $\bar{d}$ quark and the electron in the center-of-mass frame. The transverse momentum $\hat{p}_T$ of the e^+(or ν_e) is:

$$\hat{p}_T^2 = \frac{1}{4}\hat{s}\sin^2\hat{\theta} \tag{2.26}$$

or

$$\cos\hat{\theta} = \sqrt{1-4\frac{\hat{p}_T^2}{\hat{s}}} \tag{2.27}$$

Changing variables from $d\cos\hat{\theta}$ to $d\hat{p}_T^2$ by introducing

$$\frac{d\cos\hat{\theta}}{d\hat{p}_T^2} = -\frac{2}{\hat{s}\sqrt{1-\frac{4p_T^2}{\hat{s}}}} \tag{2.28}$$

into Eq.(2.22), we have:

$$\frac{d\hat{\sigma}}{d\hat{p_T}^2} = \frac{|V_{ud}|^2}{\pi}(\frac{G_F M_W^2}{\sqrt{2}})^2 \frac{1}{(\hat{s}-M_W^2)^2+(,_W M_W)^2}\frac{1-2\hat{p}_T^2/\hat{s}}{(1-4\hat{p}_T^2/\hat{s})^{1/2}} \tag{2.29}$$

The divergence at $\hat{p}_T = \sqrt{\hat{s}}/2 \simeq M_W/2$ stems from the *Jacobian*, Eq. 2.28, and is known as the *Jacobian Peak*. This is at the parton level. The divergence is removed after the parton distributions are folded in and averaged over the Breit-Wigner shape. This leaves the *Jacobian Peak* with finite height.

The inclusive hadronic cross section for $p\overline{p} \longrightarrow e^+\nu_e$ has the form:

$$d\sigma(P\overline{P} \longrightarrow e^+\nu X) = \frac{1}{3}\sum_{q,q'}\int_0^1 dx_a \int_0^1 dx_b q(x_a)\overline{q}'(x_b)d\hat{\sigma}(q\overline{q}' \longrightarrow e^+\nu) \qquad (2.30)$$

where $q(x_a)$ is the probability of finding a parton in the proton carrying fraction x_a of the proton's momentum. The summation is over both quarks and antiquarks. The subprocess cross section, $d\hat{\sigma}$, is given by Eq.(2.29), with $\hat{s} = x_a x_b s$, where s is the $p\bar{p}$ center of mass energy. The parton distributions are evaluated at $Q^2 = \hat{s} = M_W^2$.

2.3 W Mass Measurement Technique

The advantage of using the *Jacobian Peak* to measure the W mass was realized and studied in [13]. The location of the *Jacobian Peak* in the electron transverse momentum spectrum is sensitive to the W mass, and the fall off at high P_T, near half the W mass, is sensitive to the width. The data in the region of the peak can be compared to a Monte Carlo simulation to extract the W boson mass.

It can be shown that there is also a *Jacobian Peak* in the W transverse mass distribution. The W transverse mass is defined in the plane transverse to the $p\overline{p}$ beams in a manner analogous to the invariant mass:

$$m_T^2(W) = (P_T(e) + P_T(\nu))^2 - (\vec{p}_T(e) + \vec{p}_T(\nu))^2 \qquad (2.31)$$

It can be rewritten as

$$m_T^2(W) = 2P_T(e)P_T(\nu)(1 - \cos\phi_{e\nu}) \qquad (2.32)$$

where $\phi_{e\nu}$ is the angle between the electron and neutrino in the transverse plane. Since the neutrino is not directly measurable in the detector, it is signaled by the presence of large missing transverse momentum ($\not{P}_T$).

When the W is produced with zero p_T, which is roughly true for most W's, the transverse mass is given simply by:

$$m_T(W) = 2|\vec{p}_T(e)| = 2|\vec{p}_T(\nu)| \qquad (2.33)$$

Combining Eq.2.33 and Eq.2.29, we have:

$$\frac{d\hat{\sigma}}{d\hat{m_T}^2} = \frac{|V_{ud}|^2}{4\pi}(\frac{G_F M_W^2}{\sqrt{2}})^2 \frac{1}{(\hat{s} - M_W^2)^2 + (,_W M_W)^2} \frac{2 - \hat{m_T}^2/\hat{s}}{(1 - \hat{m_T}^2/\hat{s})^{1/2}} \tag{2.34}$$

The divergence at $\hat{m}_T = \sqrt{\hat{s}} \simeq M_W$ is again removed after folding in the parton distributions and averaging over the Breit-Wigner shape.

However, the W can also be produced with a finite longitudinal momentum p_L^W and transverse momentum p_T^W. Taking the transverse momentum of the W along the x direction and the longitudinal momentum along the z direction, we have

$$\beta_x = \frac{p_T^W}{E_W} \tag{2.35}$$

$$\beta_z = \frac{p_L^W}{E_W} \tag{2.36}$$

where E_W is the total energy of the W. Using primes to denote cm variables, the Lorentz transformation for the electron is :

$$E_e = \gamma(E'_e + \beta_x p'_{xe} + \beta_z p'_{ze}) \tag{2.37}$$

$$p_{xe} = p'_{xe} + \frac{\gamma - 1}{\beta^2}\beta_x^2 p'_{xe} + \gamma\beta_x E'_e \tag{2.38}$$

$$p_{ye} = p'_{ye} \tag{2.39}$$

$$p_{ze} = p'_{ze} + \frac{\gamma - 1}{\beta^2}\beta_z^2 p'_{ze} + \gamma\beta_z E'_e \tag{2.40}$$

and for the neutrino is:

$$E_\nu = \gamma(E'_\nu + \beta_x p'_{x\nu} + \beta_z p'_{z\nu}) \tag{2.41}$$

$$p_{x\nu} = p'_{x\nu} + \frac{\gamma - 1}{\beta^2}\beta_x^2 p'_{x\nu} + \gamma\beta_x E'_\nu \tag{2.42}$$

$$p_{y\nu} = p'_{y\nu} \tag{2.43}$$

$$p_{z\nu} = p'_{z\nu} + \frac{\gamma - 1}{\beta^2}\beta_z^2 p'_{z\nu} + \gamma\beta_z E'_\nu \tag{2.44}$$

From these equations we may calculate the transverse mass in the laboratory frame in terms of the c.m. frame quantities. The result is:

$$m_T^2(W) = m_T^{'2}(W)(1 + O(\beta_x^2)) \tag{2.45}$$

We can see that the transverse momentum of the W, p_T^W, affects the transverse mass only at order $\beta_x^2 \approx (p_T^W/m^W)^2$, while it affects the electron p_T more directly. So the *Jacobian Peak* is smeared out more in the electron p_T distribution than in the W transverse mass distribution. The spectrum shape is then less sensitive to the W mass. In addition, there are errors introduced by the theoretical uncertainties in the P_T^W spectrum. There is, therefore, a big advantage to using the distribution in W transverse mass to determine the W mass. Of course, both electron and neutrino p_T distributions can be used to cross check the W mass measurement.

Chapter 3

The DØ Detector

The DØ Detector was designed and constructed to study proton-antiproton collisions at the Fermilab (Fermi National Accelerator Laboratory, FNAL) Tevatron Collider. The preliminary physics focus is the study of high mass states and high P_T phenomena. The DØ detector was optimized with the following three general goals in mind:

- Excellent identification and measurement of electrons and muons.
- Good measurement of parton jets at high P_T using a highly segmented calorimeter with good energy resolution.
- Good resolution in missing transverse momentum ($\not{P}_T$) to detect the presence of neutrinos and other noninteracting particles.

A cutaway isometric view of the detector is shown in Fig. 3.1. The detector consists of a tracking system, a calorimeter to measure the energies of electrons, photons and jets, and a muon system to identify muons and measure their momenta. Included among the detector subsystems are:

- a Vertex Drift Chamber (VTX)

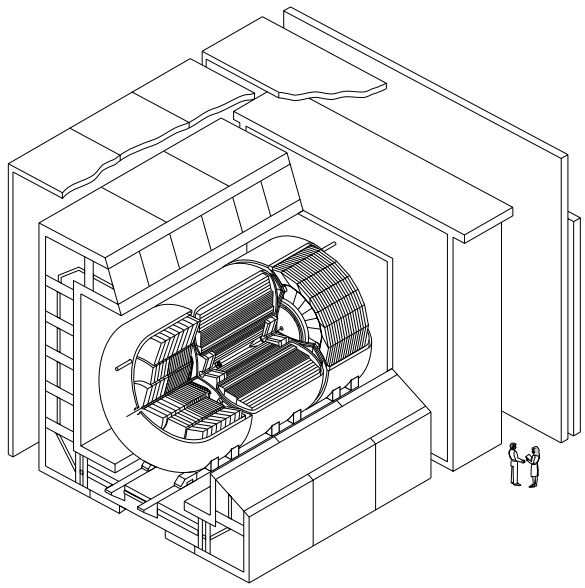

/

Figure 3.1: The DØ Detector

- a Transition Radiation Detector (TRD)
- Central and Forward/Backward Drift Chambers(FDC)
- Central and End Calorimeters(EC) and
- a Muon Detector.

A brief description of each sub-detector will be given in the following paragraphs.

3.1 Central Tracking(CD)

3.1.1 Vertex Detector(VTX)

The VTX chamber is the innermost tracking detector. It is 80 cm long, centered on the interaction region, and begins just outside the beryllium beam pipe at $r = 3.7\ cm$. The active region extends radially to $r = 16.2\ cm$.

The typical resolution is 50 μm in the $r-\phi$ direction and 1 cm in the z direction.

3.1.2 Transition Radiation Detector(TRD)

The TRD occupies the annulus between the VTX and CDC and provides added, independent electron identification to the very good discrimination already provided by the calorimeters. The ability to discriminate electrons from hadrons has been studied in detail in a test beam[16]. Use of the total energy alone gives a factor of 10 rejection of pions while retaining 90% of the electrons. The rejection factor increases to 50 using a likelihood analysis, without further loss in electron efficiency.

3.1.3 Central Drift Chambers(CDC)

The CDC provides coverage for tracks at large angles, i.e. $40^o < \theta < 140^o$. It is a cylindrical shell of length 184 cm and inner and outer radii of 49.5 cm and 74.5 cm. The $r-\phi$ and z-coordinate measurements are made using four concentric rings of detectors, each containing 32 azimuthal cells. In each cell there are seven 30 μm gold-plated tungsten sense wires that run parallel to the z-axis and provide the $r-\phi$ measurement. Two delay lines located just before the first, and after the last, sense wire are used to measure the z-coordinate. The CDC is operated with $A_r(93\%)CH_4(4\%)CO_2(3\%)$ gas with 0.5% H_2O. The inner sense wires are maintained at a voltage of 1.45 kV and the outer sense wires are held at 1.58 kV.

The $r-\phi$ resolution is about 150 μm and the z-resolution is $\sigma_z \simeq 2\,mm$. The rejection of two overlapping tracks is in the range of 75 to 100, while the efficiency for retaining single tracks, using the CDC and the VTX, is 98%.

3.1.4 Forward and Backward Drift Chambers(FDC)

The FDC's extend the coverage for charged particle tracking to within $\theta \simeq 5^o$ of the beam axis. These chambers are located at either end of the concentric barrels

of the VTX, TRD and CDC. Each FDC consists of three separate chambers: the Φ module whose sense wires are radial and measure the ϕ coordinate, sandwiched between a pair of Θ modules whose sense wires measure the θ coordinate. FDC chambers are operated with the same gas as the CDC. The $r-\phi$ resolution is about 200 μm. The resolution in z is $\sigma_z \simeq 4\,mm$.

3.1.5 Read Out Electronics

The readout electronics for central detectors are almost all the same. There are three stages of signal processing: the preamplifiers mounted directly on the chambers themselves, the shapers located in the detector platform, and the flash ADC digitizers located about 20 meters away from the detectors. Hardware zero suppression is employed to reduce the amount of data transmitted and and to increase transfer speed.

3.2 Calorimeter

Calorimetry is essential for the W boson mass measurement. It provides the energy measurement, and plays an important role in identifying electrons, photons and jets. It also provides the measurement of missing transverse momentum to signal the presence of neutrinos, which would otherwise go undetected. The DØ calorimeter, shown in Fig 3.2, was designed to be nearly compensating, responding equally to hadrons and electrons (e/h=1.05) [17], This results in an excellent measurement of the energy of incident hadrons. It is achieved using liquid argon as signal sampling material and uranium as absorber. The calorimeter covers almost the entire 4π of solid angle. Fig. 3.3 shows one quadrant of the detector and indicates clearly the calorimeter coverage in pseudorapidity (η) [30]. The region $|\eta| < 1.1$ is covered by the Central Calorimeter(CC). The two end calorimeters, ECN and ECS, extend the η coverage to $|\eta| \simeq 4.5$.

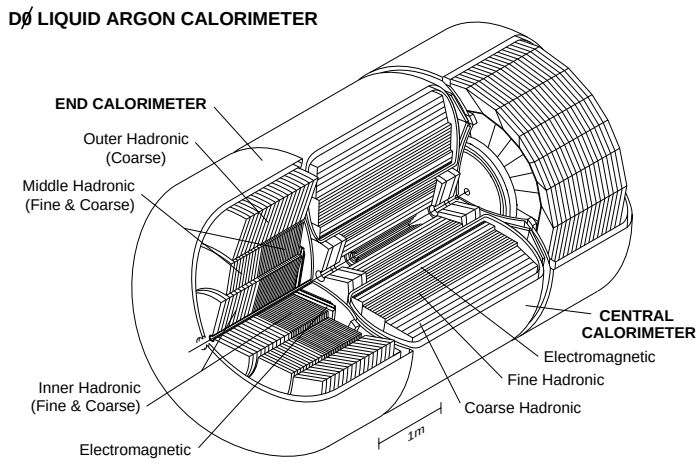

Figure 3.2: Calorimeter

3.2.1 Central Calorimeter

The central calorimeter(CC) is contained in one cryostatic vessel. It consists of three concentric cylindrical shells. There are 32 electro-magnetic(EM) modules in the inner ring, 16 fine hadronic(FH) modules in the surrounding ring and 16 coarse hadronic(CH) modules in the outer ring. Uranium is used as the absorber for the EM and FH modules, and copper is used for the CH modules. Located on either side of each uranium plate is a signal board, which collects the deposited charge on copper pads and transmits it to connectors at the ends of the modules. The gap between the uranium plates and the signal boards, the region filled with liquid argon, is 2.3 mm.

Each EM module covers 0.2 radians in ϕ and is divided into 4 radial segments of approximately 2.0, 2.0 ,6.8 and 9.8 radiation lengths(X_0). The readout tower size is 0.1×0.1 in $\Delta\eta \times \Delta\phi$. The third layer, near the shower maximum, is further divided

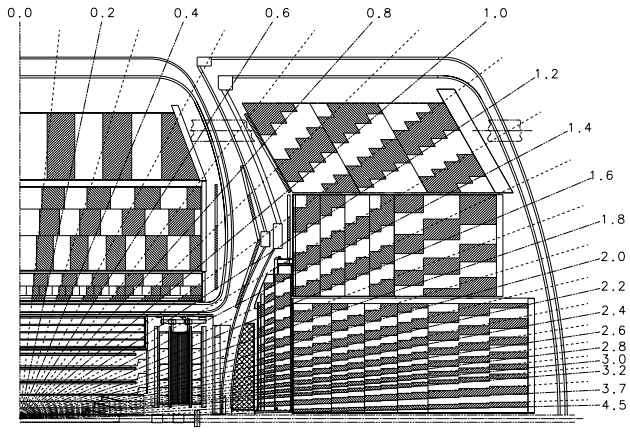

Figure 3.3: Calorimeter η coverage

into 0.05×0.05 pads in order to give good shower shape and position measurement.

The FH modules have three radial segments of approximately 1.3, 1.0, and 0.9 interaction lengths(λ_A). The CH modules, 3.2 λ_A thick, have no radial segmentation. The η, ϕ segmentation is also 0.1×0.1.

There are about 15,000 signal readout channels in the Central Calorimeter.

3.2.2 End Calorimeters

The two mirror-image end calorimeters(ECN and ECS) extend the coverage down to η =4.5 — 5.2. There are four types of modules in each of the EC's. The EM module and the inner hadronic(IH) module are designed as single units which cover the entire aperture. Outside the EM and IH, there are middle and outer (MH and OH) rings of 16 modules each.

The EM module has 0.1×0.1 readout towers in $\Delta\eta \times \Delta\phi$ space. The third layer is subdivided into 0.05×0.05 towers, as in the CCEM modules. In the radial direction, it is divided into 4 depths of 2.6, 2.6, 7.8, and 10.4 radiation lengths.

The hadronic modules have the same η, ϕ segmentation as the EM modules. There are four depths that total about $4\lambda_A$ in the fine hadronic portion and one depth in the coarse hadronic portion, also of $4\lambda_A$. In the two end calorimeters there are approximately 30,000 channels.

3.2.3 Intercryostat Detectors

Since the DØ calorimeter is divided into three independent cryostats, the regions in between the cryostats contain some amount of uninstrumented material. To obtain some measure of the energy deposition in these areas, two scintillation counter arrays, the intercryostat detectors(ICD), are mounted on the front surfaces of the EC's. Each ICD consists of 384 scintillator tiles of size $\Delta\eta \times \Delta\phi = 0.1 \times 0.1$. In addition, separate single-layered massless gaps(MG) are installed in the region of overlap of the CC detector and each of the EC's. Together, the ICD's and massless gaps provide a good approximation to the standard DØ sampling of EM showers in these difficult to cover regions.

3.2.4 Calorimeter Readout Electronics

Signals from the calorimeter modules are brought to cryostat feedthrough ports by 30Ω coaxial cables and connected to the 27 layer printed circuit feedthrough boards. The feedthrough boards are responsible for reordering the module oriented input signals into η — ϕ tower oriented outputs. This way, each preamp board hosts one trigger tower of size $\Delta\eta \times \Delta\phi = 0.2 \times 0.2$.

Liquid Argon signals go directly to charge sensitive preamplifiers, located in shielded enclosures mounted directly on the cryostats. There are two kinds of amplifiers with different gains to provide the full dynamic range. The variation in the amplifier gains of a given type is about $1 \sim 2\%$. This is further calibrated to within 0.25% by a calibration pulser system.

Output signals from the preamplifiers are transported on 110Ω twisted pair cable some 25 meters to circuits which shape the signals and subtract the baseline (BLS's). The signals are integrated($RC = 430ns$) and differentiated ($RC = 33\mu s$) and amplified by a factor of ~ 3. After shaping, the signal is sampled twice, just before the beam crossing and $2.2\mu s$ after. The difference, which is proportional to the collected charge, is obtained as a DC voltage. Two storage capacitors for each channel allow double buffering at the analog level. The output is sent to a comparator which senses the signal amplitude. Signals less than one eighth the dynamic range of the analog to digital converter (ADC) are boosted by a precision $\times 8$ DC amplifier. A bit is set to record which signals are amplified. By this method, 15 bit dynamic range is achieved with an economical, 12 bit successive approximation ADC.

Each BLS mother board hosts the 48 channels that form a $\Delta\eta \times \Delta\phi = 0.2 \times 0.2$ trigger tower. In parallel with the main signal processing, a part of the input signal to the BLS card is extracted, differentiated and sent on to the trigger system. The EM and hadronic channels of a trigger tower are added separately and the sums are used for fast, Level 1, event selection.

The main BLS signals are multiplexed 16-fold onto the crate backplanes. The signals are sent, 24 at a time in 16 serial times slices, over 50 meter cables to the digitization electronics. Each ADC card handles 384 channels. There are 24 channels of 12 bit ADC circuits on each card. Together with the $\times 1$ — $\times 8$ amplifiers, the overall dynamic range achieved is 2^{15}.

The gain parameters are set so that 4 MeV of deposited energy corresponds to approximately one ADC count. A minimum ionizing particle (MIP) deposits between 2 (in EM1) and 30 (in FH1) ADC counts in the layers of the calorimeter. The random electronic noise and the noise caused by the uranium radioactivity are between 5 and 10 counts. Adding all the towers that the MIP particle goes through

increases the signal linearly while the noise increases only as the square root. It is possible to measure a minimum ionizing particle in the calorimeter[18].

The system has been tested extensively, and found to be linear, stable, and reliable. The rate of failure of the signal channels in the detector is impressively low[20, 22].

3.3 Hardware and Software Triggers

For a typical instantaneous luminosity at the Tevatron, $L = 5 \times 10^{30}\ cm^{-2}\, sec^{-1}$, and an inelastic cross section of $\sigma \sim 50\ mb$, the interaction rate is $\sim 250\ kHz$. Two levels of triggering, hardware and software, are used to reduce the rate to the $1 \sim 2\ Hz$ level for data recording.

3.3.1 Hardware Trigger : Level 0 and Level 1 Trigger

The Level 0 trigger is formed from the signals that come from scintillation counters configured around the beam pipe. It is used to signal any inelastic $p\overline{p}$ collision. It also provides a fast, approximate measurement of the interaction vertex. It forms, basically, the DØ minimum bias trigger.

The Level 1 trigger is also derived from fast electronics (hardware). The calorimeter hardware trigger makes its decision to accept or reject an event in the time available between two beam crossings ,i.e. in 3.5 μs. It reduces the data rate to about $100 \sim 200 Hz$.

The Level 1 trigger inputs are fast signals from the Base Line Subtracters (BLS). Each BLS card contains all the channels of a pseudo-projective tower of $\Delta\eta \times \Delta\phi = 0.2 \times 0.2$. The EM energies and fine hadronic energies of the cells in the tower are summed separately. Coarse hadronic channels are not used in the trigger since they normally contribute more noise than signal at the fast trigger level. The summed

signals are transported through coaxial cables to the calorimeter trigger processing system, the trigger framework.

In the trigger framework, these signals are digitized and various quantities, such as the P_T of each tower, the missing P_T and the scalar E_T are calculated from lookup tables. Physics processes are triggered based on these quantities. Within the time between two beam crossings, the trigger framework decides whether the event should be rejected or digitized and transferred to the software trigger.

3.3.2 Software Trigger : Level 2 trigger

The software trigger consists of various physics filters. The trigger software runs on a farm of 50 VAX stations(VAXstation 4000 model 60). The nodes work in parallel, running identical software and handling events sequentially. The input rate from the Level 1 is $100 \sim 200 Hz$. At this stage, the full calorimeter information is available, and some limited tracking and vertex information. At Level 2 the electron and jet candidate list passed from the Level 1 is processed. For instance, the Level 2 takes the η, ϕ position of an electron candidate from the Level 1 and unpacks a 5×5 region of readout towers around it. It then uses the energy and tracking information in this region to check if the candidate satisfies P_T threshold, isolation, shower shape, and tracking requirements. If the event is of interest, it is sent to the host computer for recording. The event size is typically one million bytes. The raw data are recorded on 8mm tapes.

3.4 Offline Data Reconstruction

The data recorded on tape are all the energies in the cells of the calorimeters if their energies are beyond threshold, and the hits in the tracking chambers. It is the job of the offline data reconstruction program to unpack the information, and to form clusters from the energy depositions in the cells of the calorimeter and tracks

from the chamber hits. It then applies electron, photon, muon, jet, and missing P_T algorithms to identify these objects. The DØ offline reconstruction program, FULL_DØRECO, contains more than 100,000 lines of code. The standard (STA) output data size is about 1000 VAX blocks (500 Kbytes). It contains the complete information of the event. A data summary format(DST) is also available which is typically about 35 VAX blocks per event.

The STA outputs are normally stored on 8mm tapes, while the DST's reside on disk for fast access.

Chapter 4

Trigger and Offline Event Selection

4.1 Data Collection

The first run at the Tevatron with the D0 detector began in late April, 1992. A few weeks later the first di-jet event was seen in the new detector. In the following months, we continued to accumulate data, while working to improve detector performance. At the end of July, 1992, the Tevatron shut down for studies. After the shutdown, accelerator performance improved and the luminosity climbed to over $10^{30}\ cm^{-2}sec^{-1}$. The detector was now operating stably, and we began to accumulate data for physics analysis. Fig. 4.1 shows the integrated luminosity versus time for the remaining nine month period of the run. During the 14 month long accelerator run, known as Tevatron Run 1(a), we recorded $16.7 \pm 2.0\ pb^{-1}$ of data to tape, not counting the many special purpose runs to calibrate and study the detector. The total integrated luminosity delivered by the accelerator was 31.1 pb^{-1}, which includes the time for beam low beta squeeze and scraping.

The inefficiencies in acquiring data come primarily from two sources: deadtime

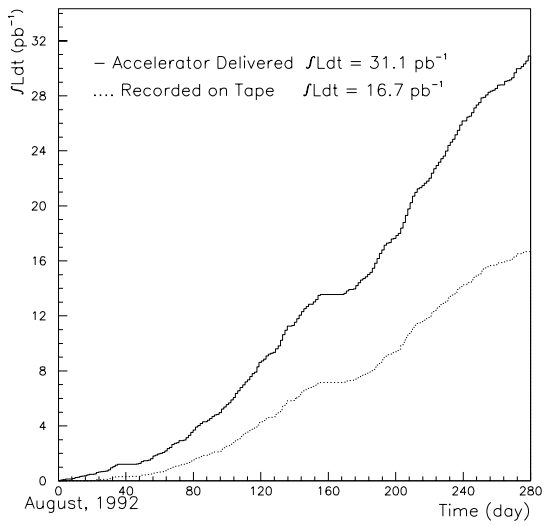

Figure 4.1: Run 1(a) Tevatron and DØ Performance.

resulting from a main ring beam veto and DØ operating inefficiency. The accelerator main ring beam pipe passes through the DØ detector. Proton-antiproton interactions that occur during the injection of beam into the main ring or when the beam in the main ring is near the DØ detector are vetoed. Events are vetoed if they occur in either of two time windows. The first veto turns the experiment off during injection, which occupies the first 400 msec of the 2.6 sec main ring cycle. This results in a 15% loss of Collider luminosity. Another veto is turned on for $1-2\mu secs$ every $20\mu secs$, the circulation time of the beam in the ring, vetoing events when the beam passes by the DØ detector. This microblanking results in an additional 5-10% beam loss. During the times these vetoes are active, energy depositions are observed in the hadronic portion of the calorimeter near the main ring beam pipe. The total loss to the main ring vetoes is about 25%. The DØ operating efficiency is 80%. After accounting the losses due to the low beta squeeze and scraping, approximately 60% of the accelerator beam is available for physics.

4.2 Online Triggers

At Level 1, the trigger for W's requires one EM tower with P_T greater than 10 GeV. For Z's, two EM trigger towers each with P_T greater than 7 GeV are required.

Level 2 works on the candidate list passed from the Level 1. For each candidate trigger tower ($\Delta\eta \times \Delta\phi = 0.2 \times 0.2$) above the P_T threshold at Level 1, the Level 2 finds the highest energy readout tower ($\Delta\eta \times \Delta\phi = 0.1 \times 0.1$) and forms a 3×3 readout tower cluster around it. A cluster of energy in the calorimeter is identified as a "trigger electron" if (1) it is isolated and 90% of the energy is in the EM section of the calorimeter and (2) the shower shape is consistent with that expected for electrons.

W events are required to have one trigger electron with a transverse momentum of at least 20 GeV. The missing P_T in the event must be 20 GeV or more. The Z candidates are required to have two trigger electrons, each with P_T greater than 20 GeV.

All events that pass Level 1 and Level 2 requirements are recorded on tape for offline analysis.

4.3 Offline Event Selection

The raw data is recorded on 8mm tapes. The events are then reconstructed offline using a 'farm' of computers. The reconstruction program finds the event vertex and the tracks which point to the energy clusters. It then calculates the cluster energies, and uses a series of algorithms to reject events in which the candidate electrons are really misidentified hadrons or jets.

4.3.1 Electron Identification

After data are recorded on tape, the offline production program (the FULL_DØRECO) employs a "nearest neighbor" algorithm for finding the electron or photon energy. An EM tower with energy greater than 1.5 GeV is used as a seed and neighboring cells over 50 MeV are added to it to form a cluster. For electron or photon candidates, the energy in the EM portion of the calorimeter must exceed 90% of the total energy, and the highest energy $\delta\eta = .1$ by $\delta\phi = .1$ tower is required to contain more than 40% of the cluster energy. The P_T of the cluster must be greater than 1.5 GeV. Electron candidates are required to have a track in the central or forward drift chambers which points from the event vertex to the cluster center.

The above criteria are required by the offline program and define an electron candidate. Additional quantities are calculated by the offline production program and made available to be used to discriminate signal from background. They may be used, or not, depending on the level of background in the particular class of events studied. **Shower shape** : The profile of energy deposition in the calorimeter, along and transverse to the candidate electron direction, must agree with that expected for an electron. In the struck $\delta\eta = .1 \times \delta\phi = .1$ tower there are eight energies measured, the energy deposited in layers EM1 and EM2, the four energies in the more finely subdivided ($\delta\eta = .05 \times \delta\phi = .05$) layer EM3, and the energies deposited in EM4 and FH1. For an electron, the energy deposited in the layers of the hadronic calorimeter beyond FH1, more than 55 radiation lengths into the shower, should be negligible even for the highest energy electrons. If one includes the 32 energies in the EM3 layer in the towers adjacent to the struck one and the z vertex, to fix the direction of the electron, there are 41 measured quantities which must agree within errors with the values expected given the electron total energy (including the energy in the FH1 layer within the cluster) and its location in the detector (described by the pseudorapidity η). The expected mean values, $\overline{x_i}$, of these quantities and the

covariance matrix

$$\sigma_{ij}(\eta, E_{tot}, Z_{vtx}) = \overline{(x_i - \overline{x_i})(x_j - \overline{x_j})} = \overline{x_i x_j} - \overline{x_i}\,\overline{x_j} \tag{4.1}$$

are obtained from Monte Carlo simulations of shower shapes which are carefully compared to data acquired in a test beam at Fermilab. For each event the χ^2 is formed:

$$\chi^2 = \sum_{i=1,j=1}^{M} (x_i - \overline{x_i})\sigma_{ij}^{-1}(x_j - \overline{x_j}) \tag{4.2}$$

and the event rejected if the χ^2 is too large. This requirement on the shower shape provides good rejection of pions, while retaining high efficiency for electrons[19].

Isolation : An isolation variable, I_{cal}, is defined using the energies measured in the calorimeter:

$$I_{cal} = \frac{E(0.4) - EM(0.2)}{EM(0.2)} \tag{4.3}$$

where $E(R)$ is the total energy deposited within the circle in (η, ϕ) space of radius $R = \sqrt{(\Delta\eta)^2 + (\Delta\phi)^2}$ and $EM(R)$ is the EM energy within the radius R.

Track match significance : A track in the central drift chamber or the forward drift chamber is normally required to point to the shower center in the calorimeter. The track match significance quantifies this requirement. In the central barrel calorimeter, using cylindrical coordinates z, ρ, ϕ, it is defined by the equation:

$$S_{trk} = \sqrt{(\frac{\Delta z}{\sigma_z})^2 + (\frac{\Delta\phi}{\sigma_\phi})^2} \tag{4.4}$$

where Δz and $\Delta\phi$ are the differences between the coordinates of the track and the calorimeter shower center at $\rho = 92cm$, the depth of the third EM layer. The σ's are the resolutions in z and ϕ. In the end calorimeters, the track match significance is defined as:

$$S_{trk} = \sqrt{(\frac{\Delta\rho}{\sigma_\rho})^2 + (\frac{\Delta\phi}{\sigma_\phi})^2} \tag{4.5}$$

where the differences $\Delta\phi$ and $\Delta\rho$ are calculated at $z = 179cm$, the depth in the end calorimeter of the EM3 layer.

4.3.2 Missing P_T Measurement

The missing P_T is defined as :

$$\vec{\not{P}}_T = -\sum_i \vec{P_T^i} \tag{4.6}$$

where P_T^i is the transverse momentum in cell i. The sum extends over all the channels in the calorimeter with signal amplitude outside a 2 σ window centered on the mean of the channel noise. Energy fluctuations in the sampling calorimeters; energy lost in and around the beam pipe and to cracks in the calorimeter; and signal fluctuations caused by the uranium radioactivity, random electronic noise, and coherent noise (pickup) all contribute to the resolution in missing P_T. Good resolution in missing P_T is achieved in the DØ calorimeter by (1) minimizing the energy fluctuations by providing good energy resolution for both hadrons and electrons in a compensating calorimeter, (2) eliminating cracks by overlapping successive rings of modules in the calorimeter, (3) reducing the energy loss near the beam pipe in the forward and backward directions by extending the calorimetry to within two degrees of the beam axis, (4) minimizing the uranium noise and random electronic noise by careful electronic design and limiting the pad sizes, and therefore cell capacitances, in the detector, and (5) carefully shielding the electronics and cables to reduce coherent noise to an insignificant level. The intercryostat regions are covered by massless gap detectors and intercryostat detectors. The coverage in solid angle is almost complete, with few uninstrumented regions.

Extensive studies were carried out to understand the noise in the calorimeter. Random noise will increase proportional to $\sqrt{N}$ where N is number of channels in the sum. Coherent noise increases linearly. For such a large system, with 50,000 channels designed to respond to charges at the femtocoulomb level, the coherent noise could easily destroy the missing P_T measurement. Many studies were carried out on subsystems of the DØ electronics and in test beams to learn how to shield

the electronics and cabling. The results of these studies were incorporated into the final design. This resulted in a system in which the coherent noise ($\propto N$) reaches the level of the random electronic noise ($\propto \sqrt{N}$) only after adding 2000 channels together. The contribution to the resolution in missing P_T is negligible[21].

From studies on the collider data, the missing P_T resolution can be parameterized by Eq. 4.7 for minimum bias events and Eq. 4.8 for di-jet events:

$$\sigma_{x,y} = 1.9 + 0.019\tilde{E}_T, \ \ (GeV) \tag{4.7}$$

$$\sigma_{x,y} = 2.0 + 0.0176\tilde{E}_T, \ \ (GeV) \tag{4.8}$$

where $\sigma_{x,y}$ is the resolution for the x or y component of the missing P_T and $\tilde{E}_T = \sum E_i sin\theta_i$ is the scalar E_T. The typical missing P_T resolution is 3.5 GeV.

4.3.3 Selection Criteria

The selection criteria are chosen to reduce the background to a relatively low level while keeping high efficiency for finding W and Z events. Care has been exercised in not biasing the measurement of the W and Z masses.

Identical requirements are imposed, when possible, on the electron and the neutrino to minimize possible selection biases, and to keep the event selection as simple as possible for ease of simulation.

Standard W mass selection cuts

The selection criteria for W events are listed in Table 4.1. These include cuts intended to identify isolated electrons and kinematic cuts to eliminate background at low P_T without greatly reducing the W signal. In order to ensure an unbiased measurement of the electron energy, the electron is also required to be away from the EM calorimeter module boundaries. The criteria for selecting electrons at the trigger level and in the offline analysis are similar, but the algorithms used are very different. In general, the offline cuts are tighter than those used in the trigger.

Electron identification
EM fraction $> 90\%$
Energy in center tower of the cluster $> 40\%$
$I_{cal} < 0.15$
$H - matrix\ \chi^2 < 100$
$S_{trk} < 10$

Kinematic cuts
Electron $P_T > 25\ GeV$
Missing $P_T > 25\ GeV$
$P_T^W < 30\ GeV$

Table 4.1: W event selection cuts

The same electron identification requirements are imposed on both electrons in the Z decay. They are each required to have a transverse momentum of at least 25 GeV.

The number of W and Z events surviving the cuts, categorized according to the location of the decay electron(s), are given in Table 4.2. (In the table, CC is the central calorimeter, $|\eta| \leq 1.1$, ECN the north end calorimeter, and ECS the south end calorimeter.) Figs 4.2 (a), (b) show the measured distributions in electron and neutrino transverse momenta for the W events surviving the cuts. Figs 4.3 (a) and (b) give the spectra in P_T^W, and W transverse mass. In the succeeding sections, we shall make use of only W and Z events with electrons detected in the central calorimeter to determine the W mass.

The cuts listed above are the standard cuts for the W and Z samples used in the mass determination. Additional cuts were imposed to study the sensitivity of the W mass to the selection criteria and to backgrounds.

Select single vertex W event

Adding the requirement that in the event only one vertex be found by the central tracking system reduces the W mass sample by 23%. The distribution in the number of vertices for W events was compared to that in a QCD sample. The QCD sample consisted of events with one high P_T EM jet and large missing P_T. These two

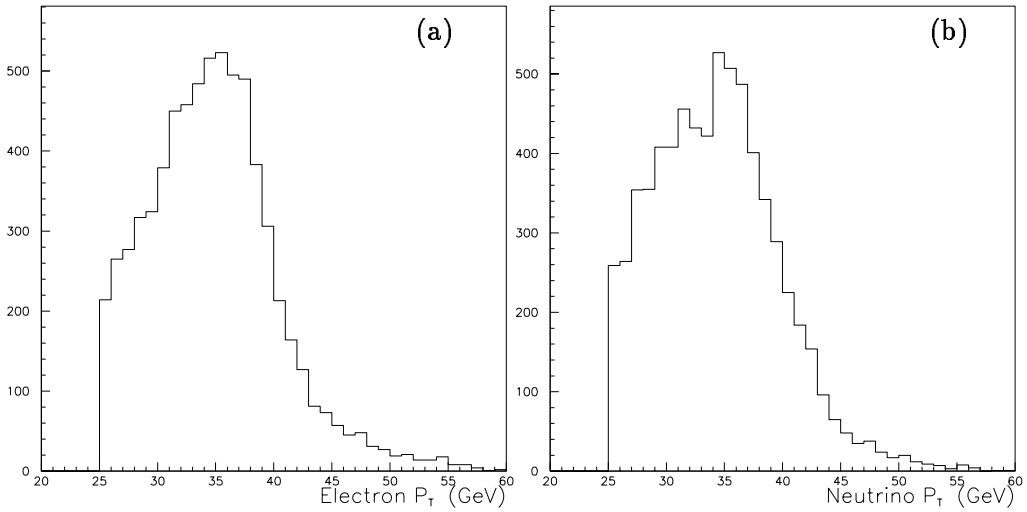

Figure 4.2: Distributions in (a) electron transverse momentum and (b) Neutrino transverse momentum.

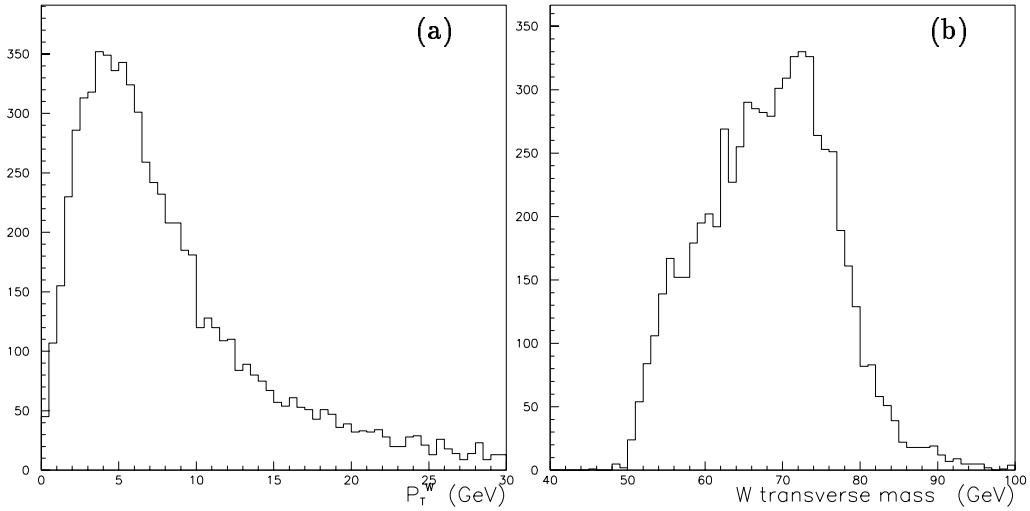

Figure 4.3: Distributions in (a) W transverse momentum and (b) W transverse mass.

W sample			*Z sample*				
ECN	CC	ECS	ECN-ECN	ECN-CC	CC-CC	CC-ECS	ECS-ECS
1522	5830	1420	34	110	313	118	28

Table 4.2: Number of W, Z events in different detector regions

samples showed similar distributions in the number of vertices, indicating that no reduction in background is achieved by imposing this cut. However, the single vertex requirement might well improve the missing P_T resolution, by reducing the total energy deposited in the calorimeter in the event. In Figs 4.4 (a) and (b) the transverse mass spectra are compared with and without the requirement of a single vertex. No improvement in resolution is visibly seen. Considering the large loss in the number of events, this cut is considered further only as a consistency check (see Chapter 8).

Cut on the number of tracks in the electron finding road

The number of central detector tracks in the electron finding road could be more than one. There are various reasons such as conversion electron tracks, low energy charge particles from the underlying event, etc. Comparing the W mass sample and the QCD sample, the requirement of a single track in the electron finding road reduces the QCD background sample by $\sim 40\%$ and the W mass sample by 13 %. Since other studies indicate that the QCD background is sufficiently low to begin with (see next section), it is not necessary to impose this cut on the data. It was used to study the dependence of the W mass on the QCD background.

Cut on the ionization in central tracking

The ionization in the central tracking system, dE/dx, can be used to reduce the background in the electron sample from neutral pions in which one or both photons from the π^0 decay convert in the central tracking system. A requirement

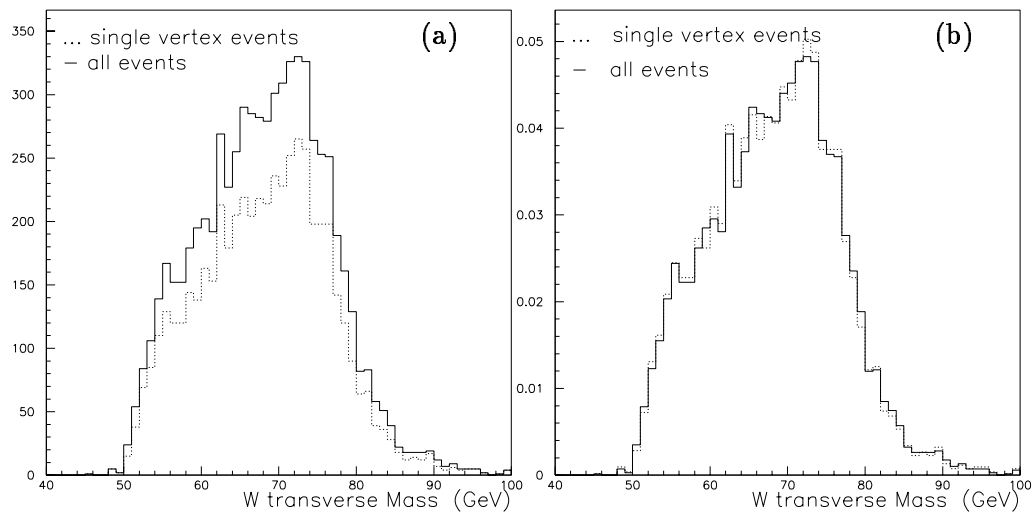

Figure 4.4: Comparison of the measured transverse mass distributions with and without the single vertex requirement. In (b) the areas of the distributions are normalized to one.

of $dE/dx < 2$ MIPs (Minimum Ionizing Particle) reduces the QCD sample by 30% and the W sample by 11%. This requirement may also be used to study the effect of QCD background on the W mass determination.

4.4 Background

The major background for $W \longrightarrow e\nu$ events are from the following sources.

4.4.1 QCD background

Hard processes in which a high P_T jet fakes an electron and the energy recoiling against the jet is lost, or partially lost, creating missing P_T, can mimic $W \rightarrow e\nu$ events. While the probability for obtaining both a large P_T electron and missing P_T in these events is small, the inclusive jet cross section for jet P_T greater than 25 GeV is 2600 nb[24], 1100 times the $W \rightarrow e\nu$ production cross section.

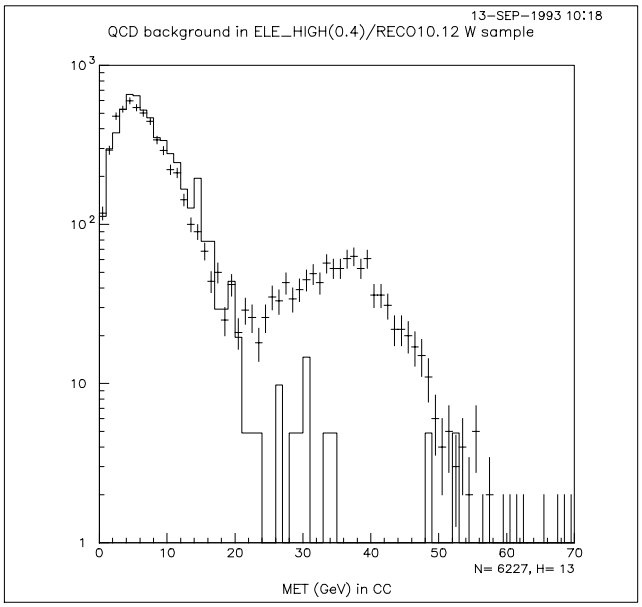

Figure 4.5: The distribution in missing P_T of the QCD background (histogram) with W events (data points with error bars) superimposed. The usual requirements on missing P_T and P_T^W are not imposed on the W events. See text for a discussion of the normalization.

The QCD background is determined directly from data. The QCD sample comes from a prescaled single EM trigger. There is no missing P_T requirement in the trigger. The EM cluster is required to pass the shape cuts normally imposed on an electron, but no isolation cut is imposed at the trigger level . The P_T threshold of the EM cluster is 16 GeV at the trigger level and increased to 25 GeV in the offline analysis. In addition, all the electron identification requirements are made on the QCD background sample that are normally made on the W events, with the exception of the isolation cut. To remove W events from the background sample, an anti-isolation cut is imposed, $I_{cal} > 0.2$. The anti-isolation cut rejects almost all the W events while keeping a substantial fraction of the QCD W-like events. The possible bias on the QCD sample from the anti-isolation requirement is studied by varying the anti-isolation cuts. This variation did not introduce significant change in the shape of the QCD background.

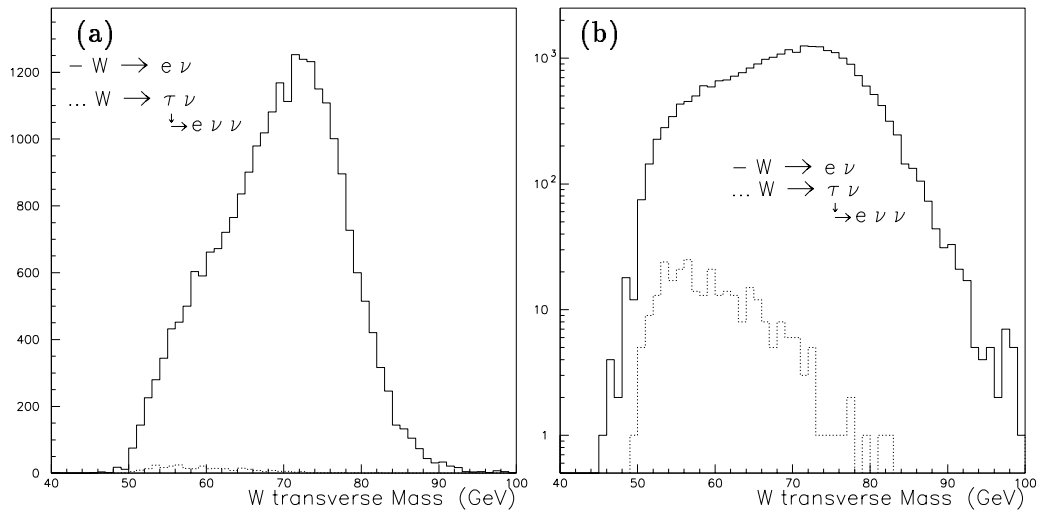

Figure 4.6: Monte Carlo generated transverse mass spectra for W's decaying directly to an electron (signal) and through tau decay (background). (a) linear vertical scale. (b) logarithmic vertical scale.

The signal sample is selected by imposing the same selection criteria stated before except there is no requirement on missing P_T and P_T^W. The signal and background samples are normalized on the missing P_T distribution for missing P_T less than 10 GeV. Fig 4.5[23] shows the missing P_T distributions of both QCD background and signal samples. After a missing P_T cut of 25 GeV, the background sample is $5 \pm 2\%$ of the signal sample. It is reduced further, to $2 \pm 1\%$, after requiring $P_T^W < 30GeV$, as in the standard W mass data set. The background is mostly at low transverse mass. The effect of this background is discussed in detail in Chapter 7. The error introduced in the W mass from the QCD background is very small.

4.4.2 $W \longrightarrow \tau\nu;\ \tau \longrightarrow e\overline{\nu_e}\nu_\tau$ Background

The W boson can decay to $\tau\nu$ and the subsequent $\tau \longrightarrow e\overline{\nu_e}\nu_\tau$ cascade will give a high P_T electron. This event type has both a high P_T electron and a large missing

P_T. It mimics the W to e ν decay. The branching ratio for W to τ decay is the same as that of the electron channel. However, the τ can decay through both leptonic and hadronic channels. The branch ratio for $\tau \longrightarrow e\overline{\nu_e}\nu_\tau$ is only 17.93%[15]. Since the electron is from a secondary decay, the P_T is smaller than produced in direct W decay to an electron and neutrino. Therefore, the kinematic cuts on the electron P_T and the missing P_T reduce this background by a substantial amount. The impact on the W mass determination is studied using the fast Monte Carlo simulation (see chapter 6). Figs. 4.6 (a) and (b) show the transverse mass spectrum from this channel after proper kinematic cuts. It gives a background in the low traverse mass region of less than 1%. The effect on the W mass fit above 60GeV is small (see Chapter 7).

4.4.3 $Z \longrightarrow ee$ Background

One of the electrons from Z decays may go into calorimeter cracks and get lost or be misidentified as a jet, producing a non-negligible amount of missing P_T. Events of this type can also mimic $W \rightarrow e\nu$ decays. Since the Z cross section times branching ratio is a factor of 10 smaller than that of the W, this background is not expected to be very large. From Monte Carlo simulations with the full DØ detector geometry, it is found to be $0.7 \pm 0.5\%$[25]. Those events are more likely to contribute in the high transverse mass region, i.e. $M_T^W \sim 80 - 100\,GeV$, compared with QCD events and W to tau decay events. Since most of the W mass information is coming from the Jacobian edge and the very low and very high end of the transverse mass spectrum is more likely to be contaminated by background, we set our standard transverse mass fitting window to be 60 GeV to 90 GeV.

Chapter 5

Detector Energy Scale Calibration

5.1 Energy Scale Carryover From Test Beam

The absolute energy scale of the DØ detector is provided initially by test beam energy calibrations. There were two test runs to study and calibrate the calorimeter modules. In the first test, several EM and hadronic end calorimeter modules were calibrated using beams of electrons and pions. In the second, two central EM calorimeter modules and several hadronic modules were calibrated. The EM energy scale is set by using the measured relationship between the electron beam momentum and the pulse height from the calorimeter, recorded in ADC counts[26]. The calorimeter electronics in the test beam and at DØ differ somewhat, primarily in the lengths of cables used and the times at which the analog signals are sampled. They are compared by using a stable pulse generator to inject equal charges in both systems. Various other differences between the test beam and the DØ detector, such as the high voltage(HV) applied across the liquid argon gap and the measured purity of the liquid argon, are also taken into account. Using this initial energy

Source of Correction	CC	ECN	ECS
Change HV $2.5kV \longrightarrow 2.0kV$	+1.5 %	+1.6%	+1.6%
Test beam Pulser time dependence	-0.4%	-1.0%	-1.0%
Test beam beam momentum re-calibration	+0.5%	+0.1%	+0.1%
Optimization of sampling fraction	$\sim$ +2.0%	$\sim$ +2.0%	$\sim$ +2.0%
Algorithm difference (TB vs DØ)	0.1%	—	—
DØ calibration pulser instability	+0.5%	+0.5%	+0.5%
Liquid Argon temperature/purity	+1.0%	+1.2%	-1.2%
Total Correction	+5.2%	+4.4%	+2.0%

Table 5.1: Energy scale corrections

scale calibration, the measured Z mass was found to be lower than that measured by the LEP experiments. This observation triggered an extensive re-examination of the electromagnetic energy scale. Table 5.1 lists the final correction factors used in setting the energy scale. The total error is about 1.5%.

5.2 Calorimeter Azimuthal Uniformity

The DØ central calorimeter consists of 32 independent modules. None of these has been directly calibrated in a test beam. The modules were constructed with strict tolerances on absorber thickness, gap size, and other geometrical properties expected to influence the amplitude of the signal from the liquid argon. However, in the test beam studies two modules were tested, and their responses to electrons differed by 1–2%. Also, the Z mass distribution initially observed was broader, at the 2–3 sigma level, than that expected from the electron energy resolution measured in the test beam. This evidence, together with the low measured Z mass, lead us to suspect variations in the responses of the modules of the central calorimeter.

There were some studies of calorimeter uniformity using minimum bias events. These events are plentiful, but using the low energy depositions per cell of the minimum bias events, typically 50–100 MeV, it is hard to give conclusive results on

the high energy, 20–50 GeV, electron response.

High energy EM showers may be used to make a simple, unambiguous relative calibration of the modules in situ at the Collider[27]. Since the $\overline{p}p$ beams in the Tevatron are not polarized, the energy flow in the direction transverse to the $\overline{p}p$ beams should not have any azimuthal dependence. Any ϕ dependence must be the result of instrumental effects. Energy scale variations among the different calorimeter towers directly affect the energy flow distribution. We have to address two issues: (1) Is there any observable nonuniformity as a function of the azimuthal angle, ϕ? and (2) If the response is nonuniform, is the nonuniformity the result of differences in scale?

We address these two issues below, after describing briefly the method of analysis and sources of error. The results presented are from the analyses of two data samples, the first acquired during normal data taking and the second obtained during a special run at the Collider carried out explicitly for this calibration.

5.2.1 Energy Flow Method and Error Analysis

Suppose the differential P_T spectrum is a simple exponential:

$$\frac{dN}{dP_T} = \mathcal{A}e^{-\mathcal{B}P_T} \tag{5.1}$$

where $\mathcal{A}$ and $\mathcal{B}$ are constants for a fixed η, and P_T is the true energy of an EM cluster. Let P_T' be the measured transverse momentum of an EM shower. We define the relative calibration constant α_i by Eq 5.2:

$$P_T \equiv \alpha_i \cdot P_T' \tag{5.2}$$

where i is the ϕ index and α_i can be η dependent. Using Eqs. 5.1 and 5.2, we derive the measured differential P_T' spectrum as :

$$\frac{dN}{dP_T'} = \mathcal{A}\alpha_i e^{-\mathcal{B}\alpha_i P_T'}. \tag{5.3}$$

Let N_i be the number of EM particles (EM showers) over a certain measured P'_T threshold P'^0_{Ti}. We have:

$$N_i = \int_{P'^0_{Ti}}^{\infty} \frac{dN}{dP'_T} dP'_T = \frac{\mathcal{A}}{\mathcal{B}} e^{-\mathcal{B}\alpha_i P'^0_{Ti}}. \tag{5.4}$$

Requiring $N_i = N_j$, we have

$$\alpha_i \cdot P'^0_{Ti} = \alpha_j \cdot P'^0_{Tj} \tag{5.5}$$

It should be noted that Eq. 5.5 does not depend on the assumption of an exponential spectrum, and holds more generally provided $N_i = f(\alpha_i P'^0_{Ti})$. We can extract the relative calibration constants by normalizing all of the ϕ indices to one:

$$\alpha_i = \alpha_0 \cdot \frac{P'^0_{T0}}{P'^0_{Ti}} \tag{5.6}$$

where α_i is the calibration constant for the ith bin in azimuth, averaged over η.

The errors in the α_i are readily computed using Eq. 5.4:

$$\frac{\partial N_i}{\partial \alpha_i} = -\mathcal{A} P'^0_{Ti} e^{-\mathcal{B}\alpha_i P'^0_{Ti}} = -N_i B P'^0_{Ti}, \tag{5.7}$$

or, with $\alpha_i \simeq 1.0$ and $\Delta N_i / N_i = 1/\sqrt{N_i}$,

$$\begin{aligned} \delta\alpha &= \left|\frac{\Delta\alpha}{\alpha}\right| && (5.8) \\ &= \frac{1}{\mathcal{B} P'^0_{Ti}} \cdot \frac{1}{\sqrt{N_i}} && (5.9) \\ &= \frac{1}{\sqrt{\mathcal{A}\mathcal{B}} P'^0_{Ti}} \cdot e^{\frac{\mathcal{B}\alpha_i P'^0_{Ti}}{2}}. && (5.10) \end{aligned}$$

From Eq. 5.9 we can see that the error on the relative calibration constant is proportional to $1/\sqrt{N}$ as expected. It is also inversely proportional to the threshold P'^0_{Ti} and the slope of the exponential decay constant $\mathcal{B}$. $\mathcal{B}$ depends on the trigger cuts used and also on the P_T threshold (not very strongly). Fig. 5.1 shows the P_T spectrum for one type of trigger, which required, at Level I, one EM trigger tower with 5 GeV or more and, at Level II, an EM cluster with P_T in excess of 7 GeV

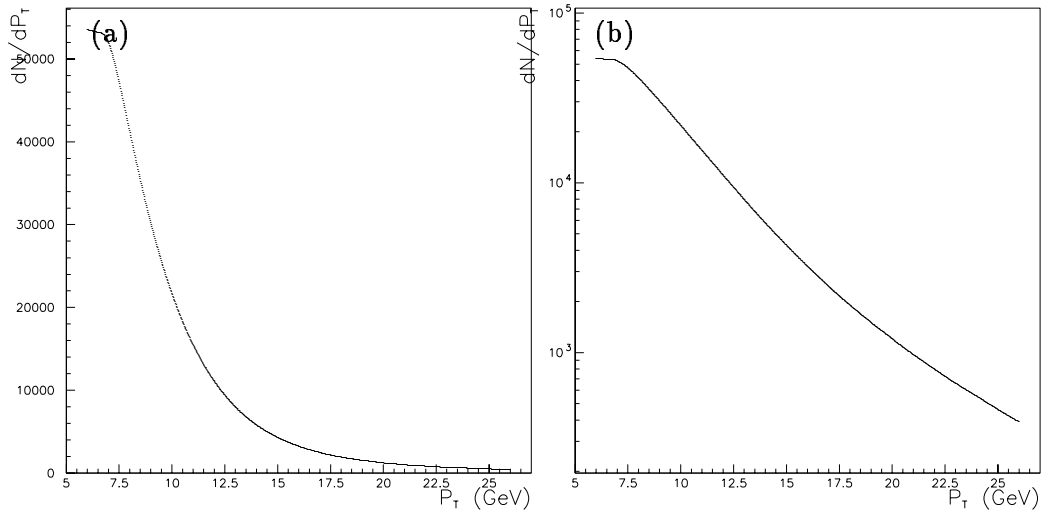

Figure 5.1: Differential P_T spectrum of EM clusters observed with special purpose trigger (a) linear vertical scale. (b) logarithmic vertical scale.

and a shower shape consistent with that expected for electrons. The fall with P_T is approximately exponential. The slope for P_T in the range from 8 to 15 GeV is $\mathcal{B} \simeq 0.2\ GeV^{-1}$. After we know the slope $\mathcal{B}$, we can choose the P_T threshold to minimize $\delta\alpha$:

$$\frac{\partial(\delta\alpha)}{\partial P_T'^0} = \frac{e^{\frac{\mathcal{B}\alpha_i P_{Ti}'^0}{2}}}{\sqrt{\mathcal{A}\mathcal{B}}P_T'^{0^2}} \cdot (\frac{\mathcal{B}\alpha P_T'^0}{2} - 1) = 0 \tag{5.11}$$

or:

$$P_{Ti}'^0 = \frac{2}{\mathcal{B}\alpha} \tag{5.12}$$

Using $\alpha \simeq 1.0$, $\mathcal{B} \simeq 0.2\ GeV^{-1}$, we find the optimum P_T threshold for this trigger: $P_T'^0 \simeq 10\ GeV$. This analysis has served as a guideline for calibration data taking.

It should be emphasized that the detector energy resolution, vertex position resolution, etc., are not taken into account in Eq. 5.9. In the case where the normalization is done to one of the ϕ indices, a factor of $\sqrt{2}$ should be taken into account,

i.e.,

$$\delta\alpha = \frac{\sqrt{2}}{\mathcal{B}P_{Ti}^{\prime 0}} \cdot \frac{1}{\sqrt{N_i}} \tag{5.13}$$

5.2.2 Simple Monte Carlo Simulation

As a test of this method, some simple Monte Carlo simulations were done with the following assumptions: (1) The differential P_T spectrum is a simple exponential with $\mathcal{B} = 0.2\ GeV^{-1}$, (2) the EM shower energy resolution is $\sigma_E/E = 16\%/\sqrt{E}$, (3) the Z vertex resolution is $\sigma_Z = 5\ cm$, (4) The EM modules are 100 cm away from the beam line, and (5) the nonuniformity in ϕ is Gaussian distributed with an rms spread of 1 %. Three different approaches were used to extract the relative calibration constants.

- *Method I*: Eq. 5.6 was used, normalizing all the the modules to a particular one.

- *Method II*: The logarithm of Eq. 5.4,

$$\log N_i = \log(\frac{\mathcal{A}}{\mathcal{B}}) - \mathcal{B}\alpha_i P_{Ti}^{\prime 0} \tag{5.14}$$

  was fit to a straight line. The slope gives information on the relative calibration constants. Although $\mathcal{A}$ and $\mathcal{B}$ can be η dependent, they cannot be ϕ dependent. We start with a linear two parameter fit to $\log N_i$ versus $P_{Ti}^{\prime 0}$ and calculate the average value of $\log(\mathcal{A}/\mathcal{B})$. After forcing $\log(\mathcal{A}/\mathcal{B})$ to be the average value, we do a one parameter linear fit to extract the slope.

- *Method III*: The average measured P_T over a given $P_{Ti}^{\prime 0}$ threshold for each ϕ index is:

$$\overline{P_{Ti}^{\prime}} = \frac{\int_{P_{Ti}^{\prime 0}}^{\infty} P_{Ti}^{\prime} \frac{dN}{dP_T^{\prime}} dP_T^{\prime}}{\int_{P_{Ti}^{\prime 0}}^{\infty} \frac{dN}{dP_T^{\prime}} dP_T^{\prime}} = P_{Ti}^{\prime 0} + \frac{1}{\mathcal{B}\alpha_i} \tag{5.15}$$

The quantity, $P'^0_{Ti} - \overline{P'_{Ti}}$, is proportional to the relative calibration constants. Since $\mathcal{B}$ is independent of ϕ, we have:

$$\frac{P'^0_{Ti} - \overline{P'_{Ti}}}{P'^0_{Tj} - \overline{P'_{Tj}}} = \frac{\alpha_i}{\alpha_j} \tag{5.16}$$

If we normalize to one ϕ index, we have:

$$\alpha_i = \frac{P'^0_{Ti} - \overline{P'_{Ti}}}{P'^0_{T0} - \overline{P'_{T0}}} \cdot \alpha_0 \tag{5.17}$$

All three methods are applied to the Monte Carlo simulation. The results are shown in Fig. 5.2, Figs. 5.4 (a), (b), and Fig. 5.5. We see that the calibration constants extracted track the input values very well, especially for *Method I* and *Method II*. The errors using *Method III* are expected to be larger. A detailed comparison shows a tendency toward worse statistical accuracy than that expected from Eq. 5.13. The $\sqrt{2}$ factor should be replaced by $\sqrt{3}$ in order to best describe the observed error.

5.2.3 Using All EM Triggers From Normal Data Taking

These methods were first applied to the data from the regular collider runs. Since a special purpose trigger was not designed for this analysis and a single trigger did not provide enough data, all the EM triggers which require at lease one EM cluster were used. These are the triggers used for W/Z physics, the top quark search, direct photon physics, and W + jets studies. They all require one or more EM clusters and the highest P_T threshold for the EM cluster is 20 GeV. Among the triggers, the single electron trigger designed primarily for W/Z physics, which requires one trigger electron above 20 GeV, makes up about 40% of the total 2.3 million events. The data taken for these particular triggers correspond to an integrated luminosity of $\sim 14\, pb^{-1}$.

In the offline analysis, each EM cluster is required to have (1) at least 90% of its energy in the EM calorimeter and (2) at least 40% of its energy in the central

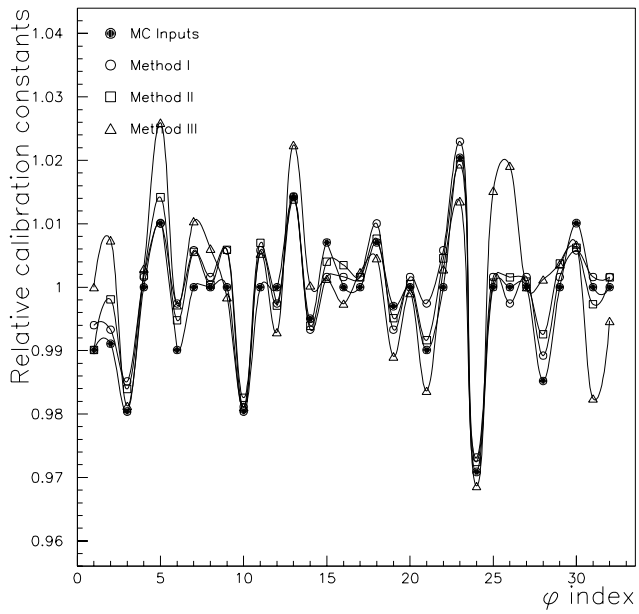

Figure 5.2: MC study. Comparison of input calibration constants to values extracted using the three methods described in text.

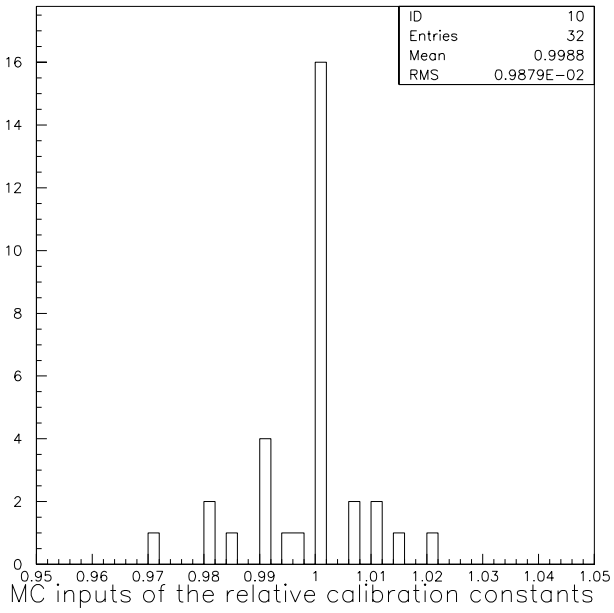

Figure 5.3: Calibration constants used as input in MC study.

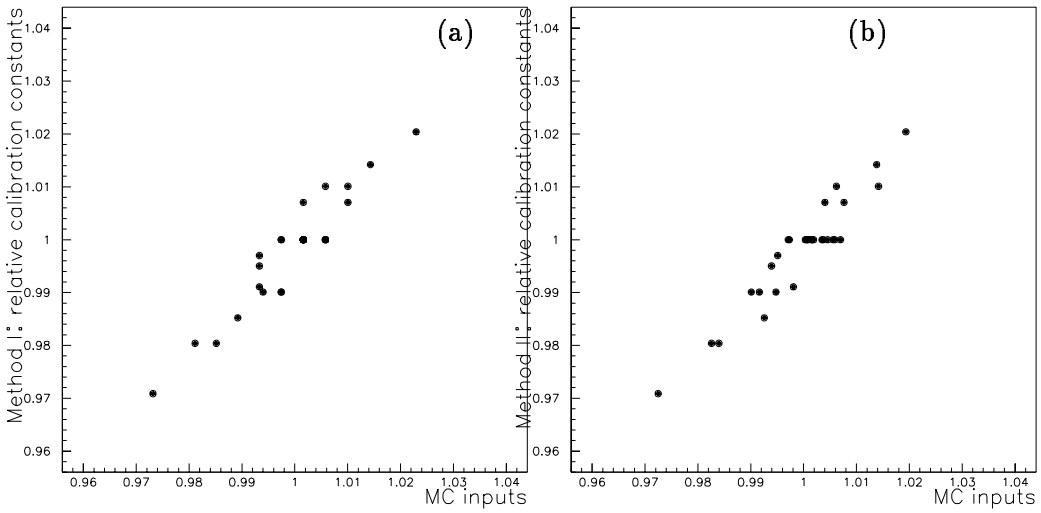

Figure 5.4: Scatter plots of the calibration constants extracted vs the MC input values. (a) Values obtained by *Method I* vs MC inputs. (b) Values obtained by *Method II* vs MC inputs.

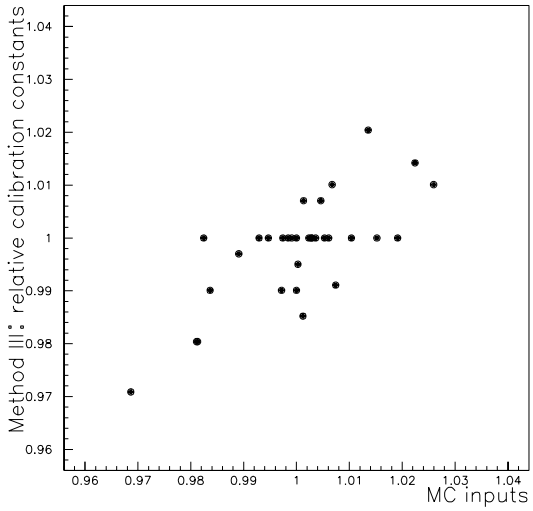

Figure 5.5: Scatter plots of the calibration constants extracted by *Method III* vs the MC input values.

$\Delta\eta \times \Delta\phi = 0.1 \times 0.1$ readout tower. Some requirements to avoid anomalous energy deposition in the calorimeter are also applied.

5.2.4 Data Set With Special EM Triggers

At the end of Tevatron Run 1(a), a special EM trigger was implemented to acquire data for the explicit purpose of studying the uniformity of the central calorimeter. The trigger was a single EM tower with 5 GeV or more P_T at the hardware level, and a cluster P_T of 7 GeV at the software trigger level. Some 3.5 million events were recorded. The results obtained from an analysis of this data permitted a determination of of the relative CC module calibration constants to .5%, and improved noticeably the W/Z mass resolution.

In the DØ detector coordinate system, module index number 1 covers ϕ from 0. to $\pi/32$, number 2 covers ϕ from $\pi/32$ to $2 \cdot \pi/32$, and so on. Fig. 5.6 (a) shows the relative calibration constants as a function of module ϕ index. No clear pattern is seen. Fig. 5.6 (b) shows the distribution of the relative calibration constants. The average value of all modules is normalized to one. Fig. 5.6 (b) shows a mean value of 1.0, as expected, and an rms deviation of all the modules of 1.3%. The maximum difference between pairs of modules is 5%.

One point worth mentioning is that the calibration constants obtained using the EM triggers of normal data taking and the constants obtained with the special purpose EM trigger are consistent. The error on the calibration constants estimated by using Eq. 5.9 is less than 0.5%. The rms of the calibration constants is 1.3% as shown in Fig. 5.6 (b).

Now we address the issue if the calibration constants are related with energy scale.

To answer the question of whether the module to module variation is related to energy scale, we divide the 32 Central Calorimeter modules into three categories

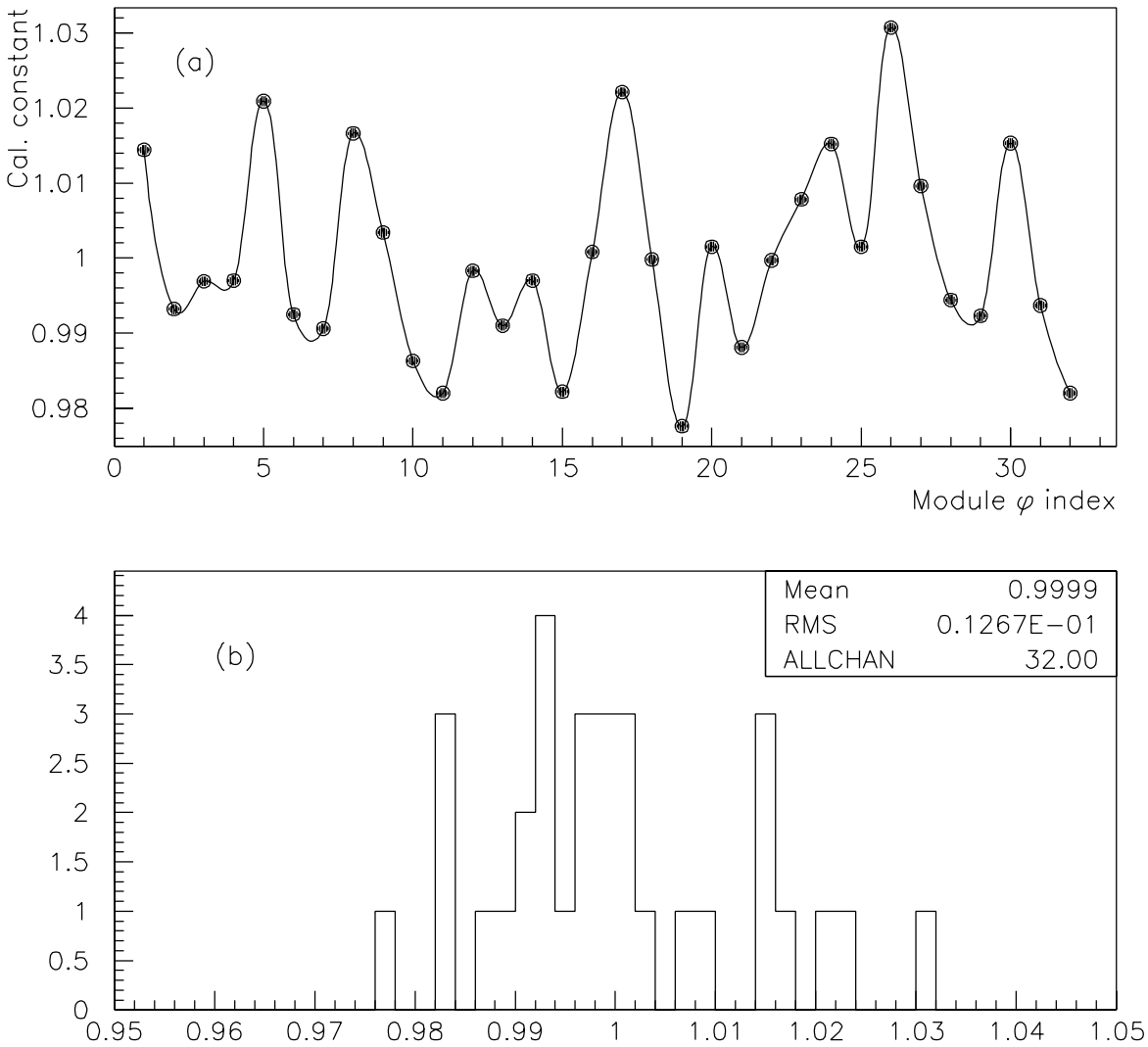

Figure 5.6: (a) Relative calibration constants for the DØ central calorimeter modules as a function of module ϕ index. (b) The distribution of the calibration constants.

High Gain Modules	Medium Gain Modules	Low Gain Modules
$\alpha_i < 0.99$	$0.99 \leq \alpha_i < 1.01$	$\alpha_i \geq 1.01$

Table 5.2: Division of three different regions according to the gain of modules.

according to their relative calibration constants, see Table 5.2. If the relative calibration constant α_i is greater than 1.01, we call it a 'low gain module' because it needs a multiplicative factor that is greater than unity to bring its gain to the true energy scale as indicated in Eq. 5.2. Medium gain modules are those with $0.99 \leq \alpha < 1.01$ and high gain modules are those with $\alpha \geq 1.01$.

Now we separate the $W \longrightarrow e\nu$ sample into three categories. If the electron is in one of the low gain modules, we put it in the low gain sample; if the electron is in one of the medium gain modules, we put it in the medium gain sample, and so on. Fig. 5.7(a) shows a comparison of the transverse mass spectra of the low gain and high gain samples before applying the relative calibration. We see that the transverse mass is shifted toward larger values in the high gain sample. Fig. 5.7(b) shows the comparison between the two samples after applying the correction to the electron energy. There is no significant difference between these two distributions. Comparisons between the medium gain sample and the low gain sample, and between the medium gain and high gain samples are shown in Figs. 5.8(a), (b) and Figs. 5.9(a), (b). Looking at the plots carefully, we conclude that the independently determined calibration constants predict the shifts in the transverse mass distributions correctly.

We can go one step further and fit the W mass for the various samples. Using Fig. 5.6 and Table 5.2, we know that the averages of the calibration constants in the high and low gains regions differs by $3.6 \pm 0.2\%$. From Table 5.3 we see that the uncorrected W masses differs by $3.2 \pm 0.8\%$. After event by event correction, the W masses differs by $-0.8 \pm 0.6\%$. We conclude that the relative calibration constants

	no correction (GeV)	with correction (GeV)
High Gain Sample	81.27 ± 0.36	79.40 ± 0.33
Medium gain sample	79.93 ± 0.20	79.84 ± 0.20
Low gain sample	78.71 ± 0.31	80.04 ± 0.33
All events	79.74 ± 0.15	79.86 ± 0.15

Table 5.3: Fits to the W mass for electrons detected in high, medium, and low gain calorimeter modules.

predict not only the direction of the shift in the W mass, but also its amplitude. This gives strong evidence that the calibration constants obtained from the energy flow method describe the energy scale variations correctly.

5.3 Z Mass Measurement And Energy Scale

The well measured Z mass at LEP serves as a useful calibration point. The Z invariant mass spectrum is a convolution of the intrinsic relativistic Breit-Wigner line shape with the detector resolution. Two different methods have been used to measure the Z mass in the DØ detector. We shall discuss them briefly below.

5.3.1 Z Mass Fitting Method I

The Z invariant mass spectrum is model by a relativistic Breit-Wigner shape with an exponential factor which accounts for the variation of the Z production cross section with Z mass in the region of the resonance[28]. The detector response is taken into account by convoluting with a gaussian response function on an event by event basis[29] . A likelihood function is formed for each measured mass m_i with associated resolution, σ_i:

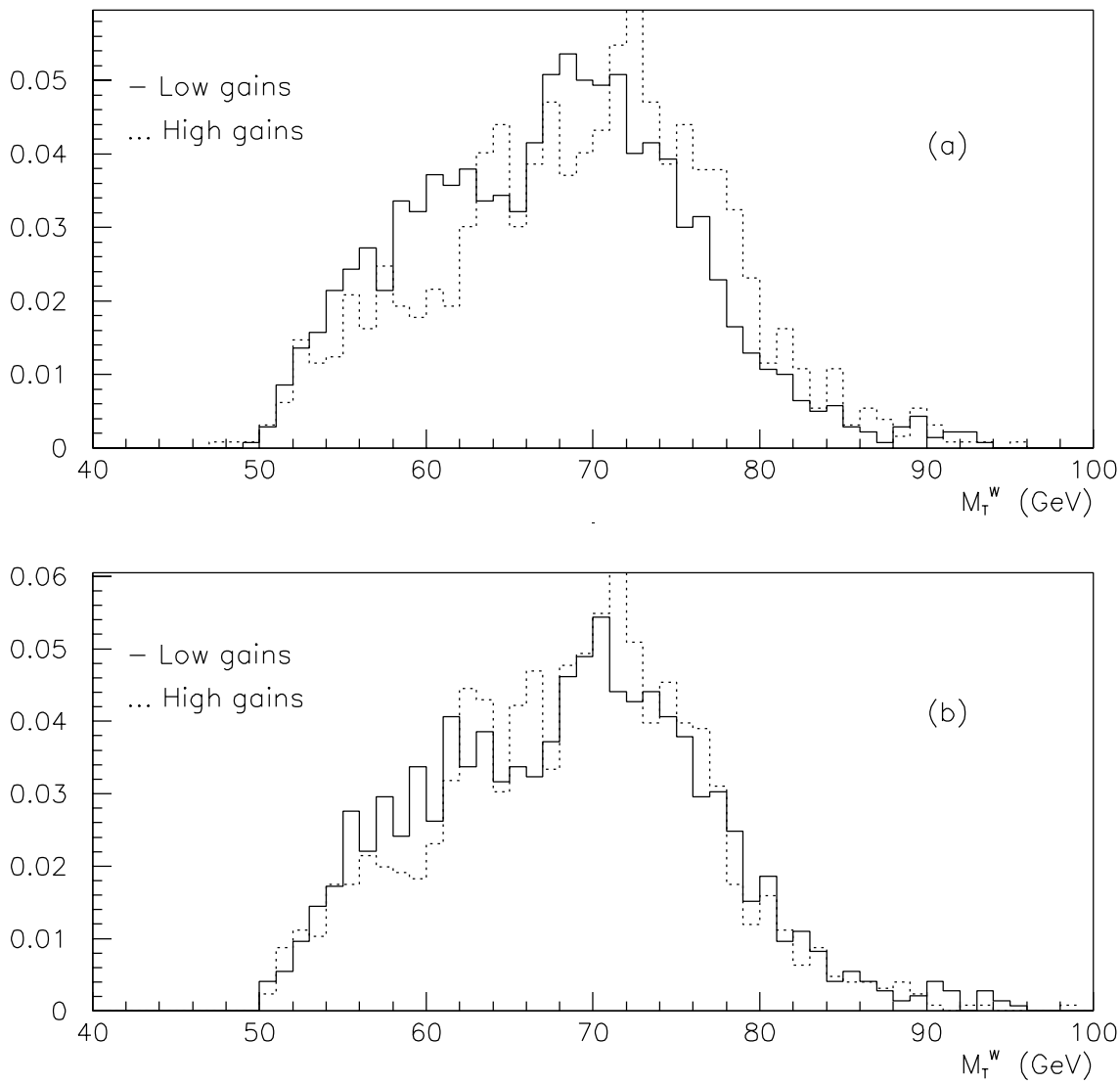

Figure 5.7: Transverse mass distributions. All distributions are normalized to unity area. (a) no correction; (b) electron energy and missing P_T are corrected by the calibration constants.

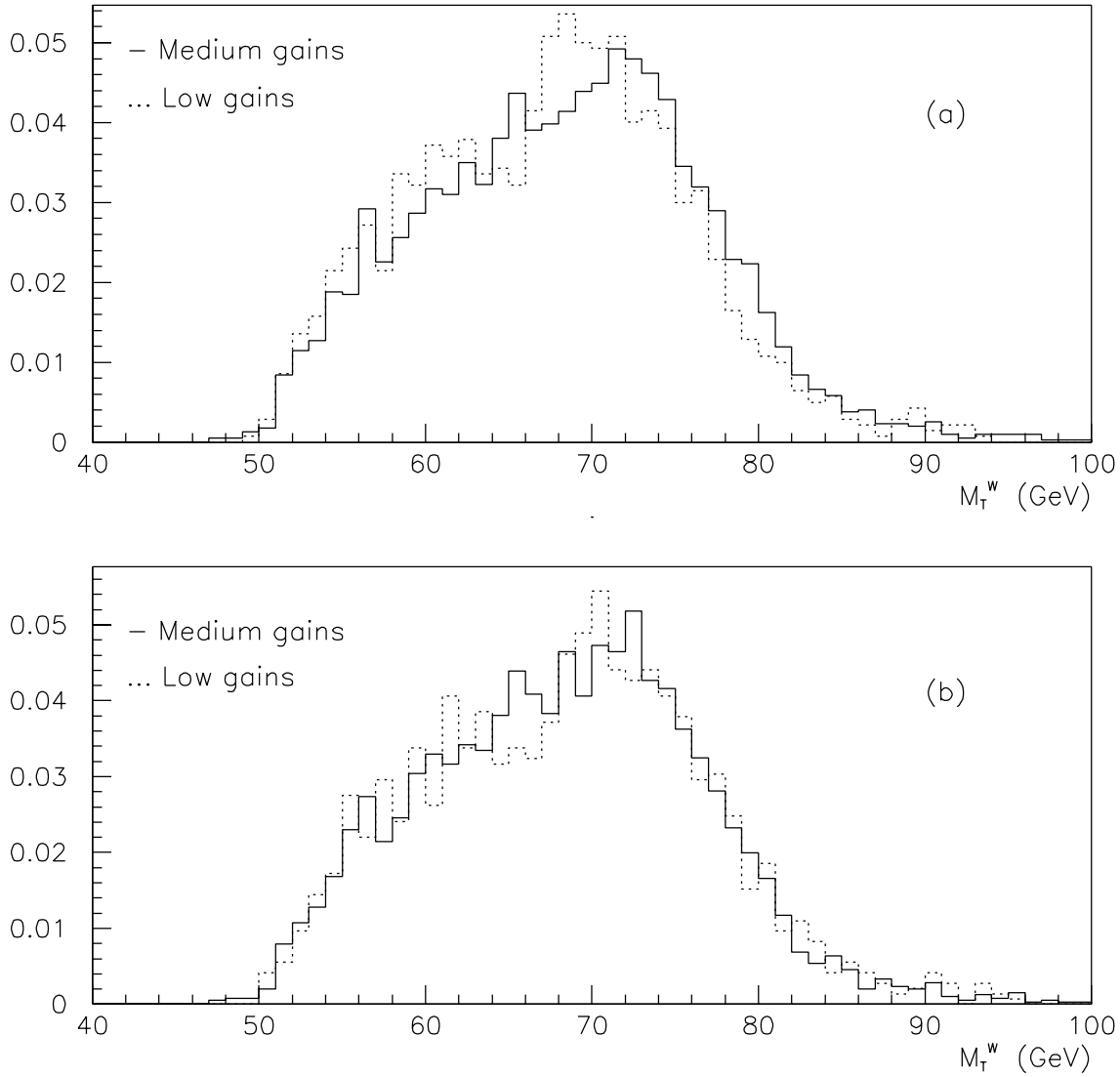

Figure 5.8: Transverse mass distributions. All distributions are normalized to unity area. (a) no correction; (b) electron energy and missing P_T are corrected by the calibration constants.

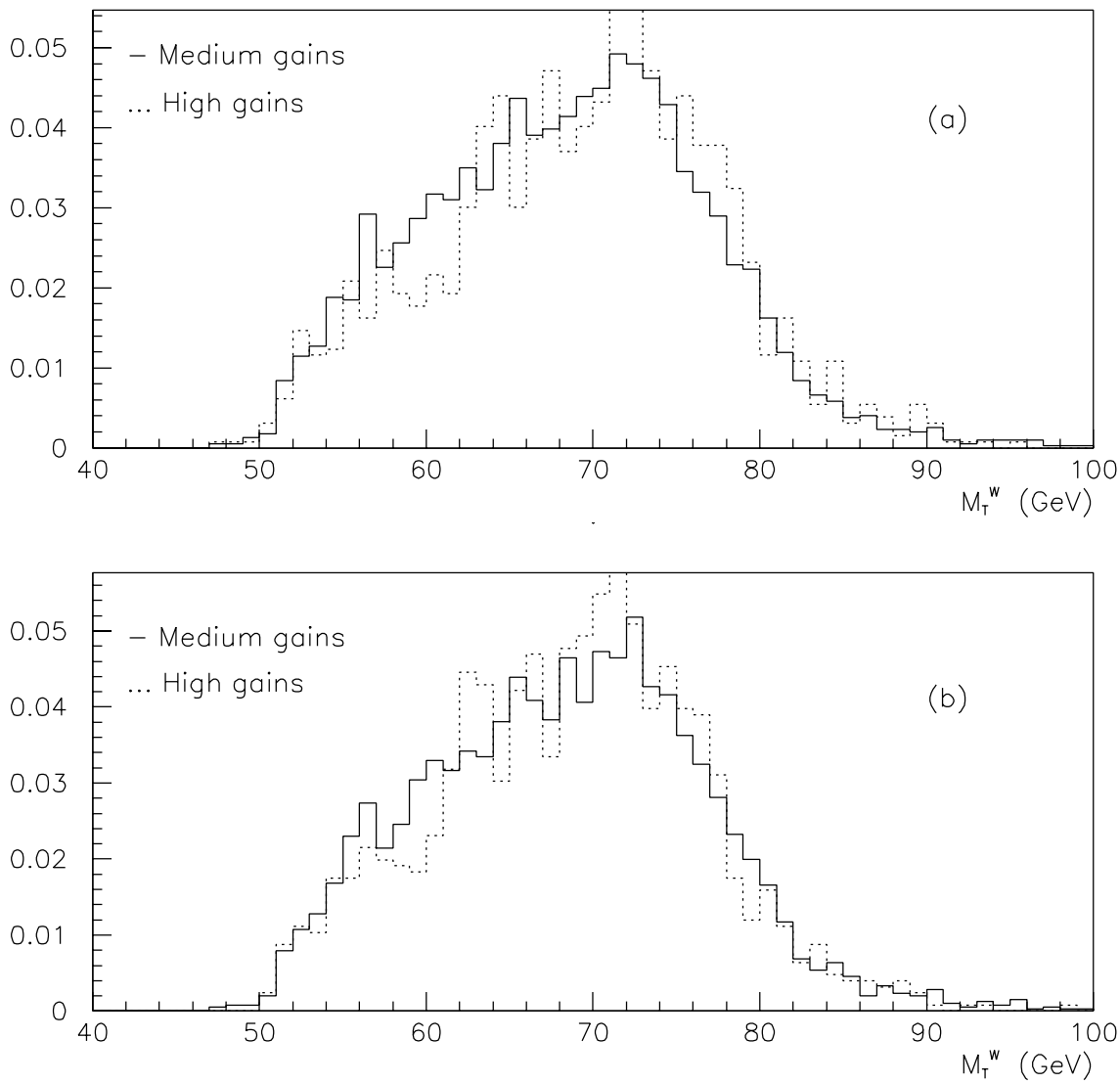

Figure 5.9: Transverse mass distributions. All distributions are normalized to unity area. (a) no correction; (b) electron energy and missing P_T are corrected by the calibration constants.

$$l(M_Z, , _Z; m_i, \sigma_i) = \int_0^\infty \left(\frac{e^{-\beta m}\ m^2}{(m^2 - M_Z^2)^2 + \frac{m^4\Gamma^2}{M_Z^2}} + \mathcal{A}e^{-\mathcal{B}m}\right) \frac{1}{\sqrt{2\pi}\,\sigma_i}\ e^{-\frac{(m-m_i)^2}{2\sigma_i^2}} \quad (5.18)$$

where M_Z and , $_Z$ are the input mass and width of the Z. A and B are used to model the background. They are determined from a fit to the dielectron invariant mass spectrum in the regions above and below the Z mass, 30-70 GeV and 100-130 GeV. The total background in the fitting window is 7%. The mass m_i is the measured mass for the ith Z event, and σ_i is the deviation expected from the event kinematics:

$$m_i = \sqrt{2E_1^i E_2^i(1 - \cos\gamma)} \quad (5.19)$$

$$\sigma_i = \sqrt{(\frac{\partial m_i}{\partial E_1^i})^2\sigma_{E_1^i}^2 + (\frac{\partial m_i}{\partial E_2^i})^2\sigma_{E_2^i}^2 + (\frac{\partial m_i}{\partial \gamma})^2\sigma_\gamma^2} \quad (5.20)$$

Here, E_1^i, E_2^i are the energies of the electrons and γ is the opening angle between the two electrons in the ith event. The electron energy resolutions, $\sigma_{E_1^i}$, $\sigma_{E_2^i}$, can be calculated from Eq.6.8, and the error in the opening angle may be determined from the uncertainties in the measured polar and azimuthal angles of each electron using the equation:

$$\cos\gamma = \sin\theta_1 \sin\theta_2 \cos(\phi_1 - \phi_2) + \cos\theta_1 \cos\theta_2. \quad (5.21)$$

The logarithm of the likelihood function, W, is formed for the events in the invariant mass window from 70 GeV to 110 GeV,

$$W(M_Z, , _Z) = \sum_{i=1}^{N} \ln \frac{l(M_Z, , _Z; m_i, \sigma_i)}{A(M_Z, , _Z)}, \quad (5.22)$$

and the Z mass obtained which maximizes W.

5.3.2 Z Mass Fitting Method II

The second method starts by generating Z events with a relativistic Breit-Wigner line shape and then performs a fast detector simulation in the same manner as for

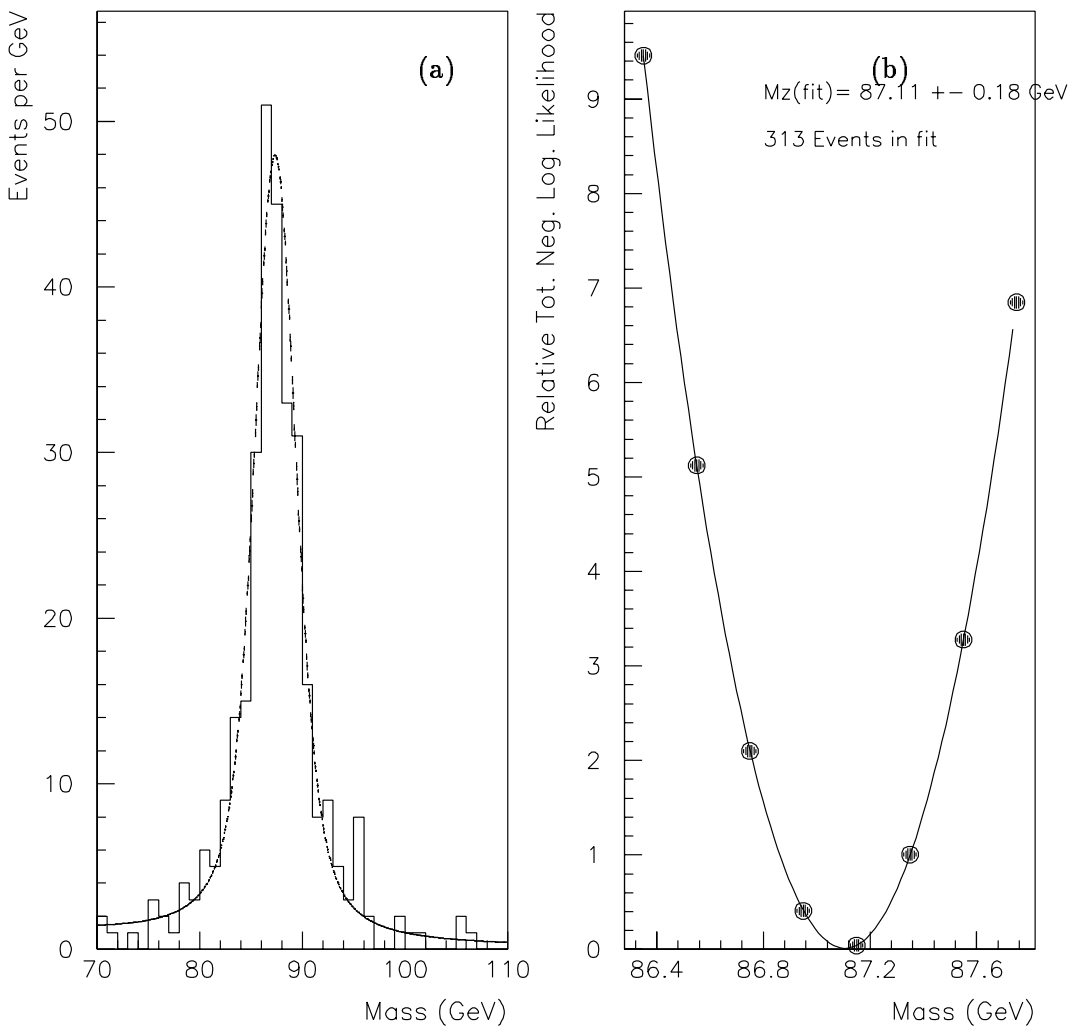

Figure 5.10: (a) The dielectron invariant mass spectrum compared to theory at the best fit value of the Z mass (b) The negative of the logarithm of the likelihood function (after moving minimum to zero) as a function of the input Z mass.

W events(see Chapter 6). The resulting Z invariant mass spectra are stored as a function of the input Z masses. They are compared with data by a maximum likelihood method and the best fit value of the Z mass obtained. Using the energy scale determined from the test beam measurements, we find:

$$M_Z = 87.11 \pm 0.18(stat)\ GeV/c^2.$$

The data are compared to theory at the best fit value of the Z mass in Fig. 5.10.

The resulting Z mass is still a few percent lower than the LEP Z mass. We now shift our energy scale up so that our measured Z mass matches that measured by the LEP experiments. We'll justify this method of setting the EM energy scale in Chapter 7 using two different methods, and also determine the scale error on the final W mass measurement.

Chapter 6

Monte Carlo Simulation Of W Events

The starting point for the Monte Carlo (MC) simulation is the double differential cross section, $d^2\sigma/dP_T^W\,dy_W$, calculated by Arnold and Kauffman[31] at next to leading order (NLO). The W produced at P_T^W, y_W according to this distribution then decays to an electron and neutrino. Proper electron angular distribution and decay kinematics are taken into account. A fast detector simulation follows.

It is not feasible to use full DØGEANT to simulate W production and decay in the DØ detector. The typical time needed for one event using full DØGEANT is 20 minutes on a typical VAX workstation[1]. It is important to study many effects which influence the measurement at the 50-100 MeV level. For instance, the presence of radiative decay, $W \rightarrow e\nu\gamma$, shifts the W mass by about 100 MeV from the value one would otherwise obtain from a fit to the spectrum in transverse mass. We would like to know this effect to about 10 MeV. The relationship between the number of

[1] A Vaxstation 4000 model 60, an 11 MIP machine

events and the statistical error can be described by the empirical relationship:

$$\Delta M_W = \frac{12}{\sqrt{N}} \, (GeV) \tag{6.1}$$

where N is the number of events used in the fit. The magic number 12 here is a result of DØ detector resolution, fiducial cuts, and event selection cuts. According to this formula, 1.44 million events are required to determine the radiative effect to 10 MeV. The typical overall yield after taking all kinematic and fiducial cuts into account is 20%, which implies following in the MC simulation 7.2 million events of 'fake' experimental data. To fit the experimental sample, we would like to have at least 10 times more statistics in the theoretical distribution than in the 'fake' experimental data. So we need to generate 72 million events. If we used full DØGEANT, it would require 2700 years running on the typical VAX workstation. Of course, there might be some tricks to reduce the requirement. But still, it is hard to imagine using the full DØGEANT to study all the effects that impact on the measurement at the 10-100 MeV level. With a fast MC simulation we can achieve a speed of 100 events per second. Only a few days running on one machine are required to study the effect on the measurement of radiative decays.

6.1 W^+ Production

A W^+ is produced by the interaction of an up (u) quark and an anti-down ($\overline{d}$) quark. (We ignore the contributions from other quark generations, i.e. Charm, Strange, Bottom, and Top, for simplicity. The following argument can be extended easily to other quark generations. Also see Fig. 6.1 caption for comments about processes: $qg \longrightarrow W^+q'$ and $\overline{q}g \longrightarrow W^+\overline{q'}$.) The quarks can come from either a valence or a sea quark in a proton and an anti-proton. Because the weak interaction of the

charged currents is left-handed in the Standard Model[2], only the interactions shown in Fig. 6.1, are allowed. There are three categories: (1) both u quark and the $\overline{d}$ are from valence quarks, Fig. 6.1(i); (2) u or $\overline{d}$ is from a valence quark and the other one is from a sea quark, Fig. 6.1(ii) and (iii); (3) both u and $\overline{d}$ are from sea quarks, Fig. 6.1(iv) and (v).

We choose the proton direction as the z axis. In the W rest frame, the decay positron angular distribution has the form $(1-\cos\theta^*)^2$ for configurations (i) to (iv) and $(1+\cos\theta^*)^2$ for configuration (v) in Fig. 6.1. Here, θ^* is the angle between the position and the z axis. For W^+, $d^2\sigma/dyd\cos\theta^*$ may be written:

$$\frac{d^2\sigma}{dyd\cos\theta^*} \sim (1+\cos\theta^*)^2 \cdot \frac{1}{2} \cdot \frac{d\sigma_s^{W^+}}{dy} + (1-\cos\theta^*)^2 \cdot (\frac{1}{2}\frac{d\sigma_s^{W^+}}{dy} + \frac{d\sigma_v^{W^+}}{dy}) \quad (6.2)$$

where $d\sigma_s^{W^+}/dy$ is for sea-sea quark contribution and $d\sigma_v^{W^+}/dy$ is for valence-valence, valence-sea quark contribution. We can write it as:

$$\frac{d^2\sigma}{dyd\cos\theta^*} \sim (1+\cos^2\theta^*) \cdot \frac{d\sigma_s^{W^+}}{dy} + (1-\cos\theta^*)^2 \cdot \frac{d\sigma_v^{W^+}}{dy} \quad (6.3)$$

In the program, we generate $d^2\sigma/dP_T^W dy$ separately for sea-sea and valence-valence/sea contributions, i.e. we start from Arnold-Kauffman distributions, $d^2\sigma_s/dP_T^W dy$ and $d^2\sigma_v/dP_T^W dy$, tabulated separately for the sea-sea and valence-valence/sea interaction. The angular distribution is then generated differently, depending on which process is involved.

Fig. 6.2 shows the double differential cross section for W^+ production as a function of the transverse momentum P_T and pseudorapidity y_W. All valence and sea quark contributions are included. Integrating the cross section over P_T, the rapidity distribution of the W^+ is obtained. It is shown in Fig. 6.3. It is interesting to note that the distribution is asymmetric for valence - valence and valence - sea contributions, i.e. configurations (i) to (iii) in Fig. 6.1 (triangle points in Fig. 6.3). There

[2]The charged currents are V-A, and the leptons which couple through charged currents are lefthanded in the zero mass limit.

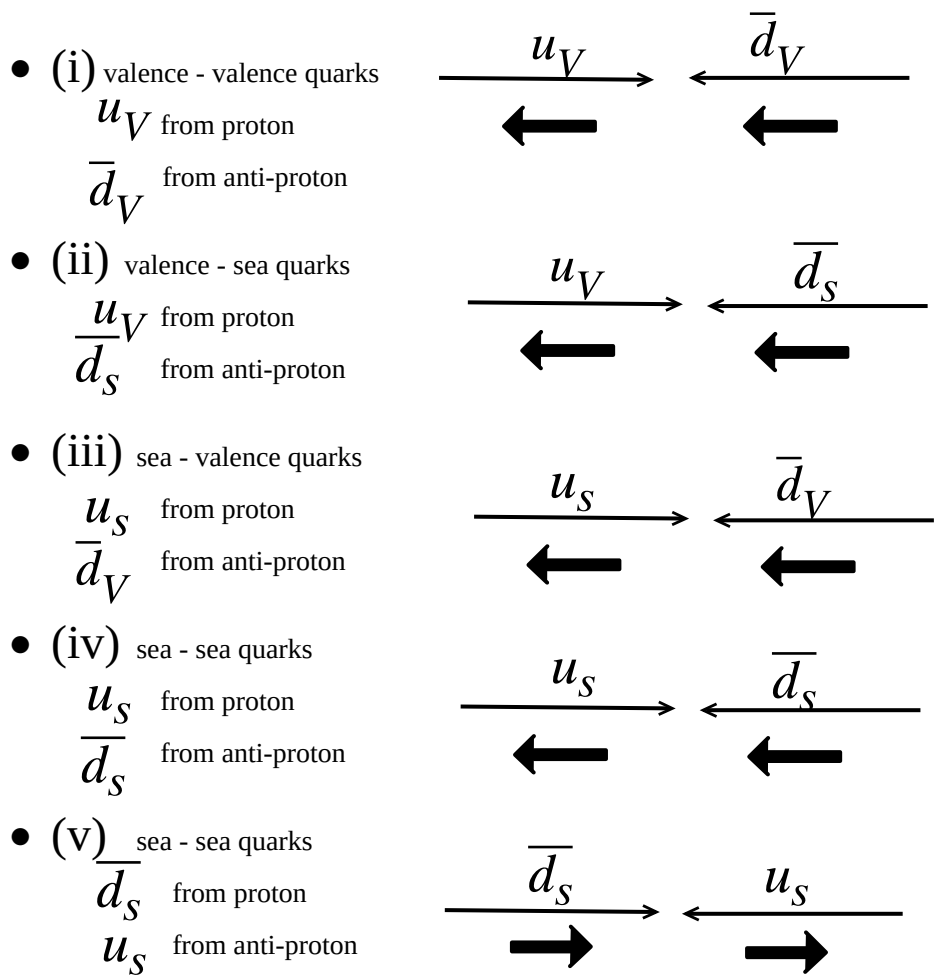

Figure 6.1: Valence and sea quark configurations for W^+ production. The light arrows indicate the momentum directions of quarks and antiquarks. The dense arrows indicate the helicities of the quarks and antiquarks. Note the contributions from processes: $qg \longrightarrow W^+q'$ and $\overline{q}g \longrightarrow W^+\overline{q'}$ can be included as part of the contributions to processes (ii) to (v).

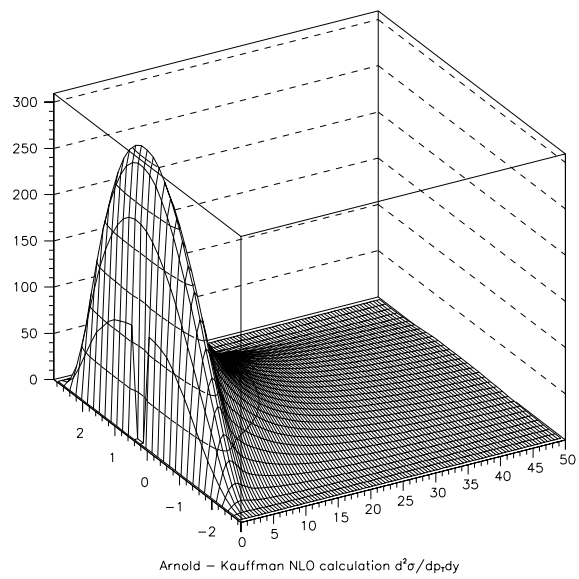

Figure 6.2: The differential cross section for W^+ production as a function of the transverse momentum P_T and pseudorapidity y.

is a shift towards positive rapidity for the W^+. The positive rapidity is defined in the proton direction. Thus there is a preference in the W production to preserve the flow of charge. This is expected in the parton model because of the difference between the structure functions of up and down quarks. Fig. 6.4 shows the structure function of u and d valence quarks; d(x) damps faster than u(x) with increasing x.

We can also see that the contribution from sea quarks, i.e. configurations (iv) and (v) in Fig. 6.1, is symmetric, as expected. In the Arnold-Kauffman NLO calculation, the sea quark contribution is 29%, which is consistent with the result in [3].

Integrating the double differential cross section over the W rapidity, we obtain the P_T spectrum shown in Fig. 6.5(a). The three curves with different valence and sea quark contributions are normalized to the same area. We see that the P_T distribution is not sensitive to the various quark contributions. Therefore, we conclude that it is not very sensitive to the choice of structure functions.

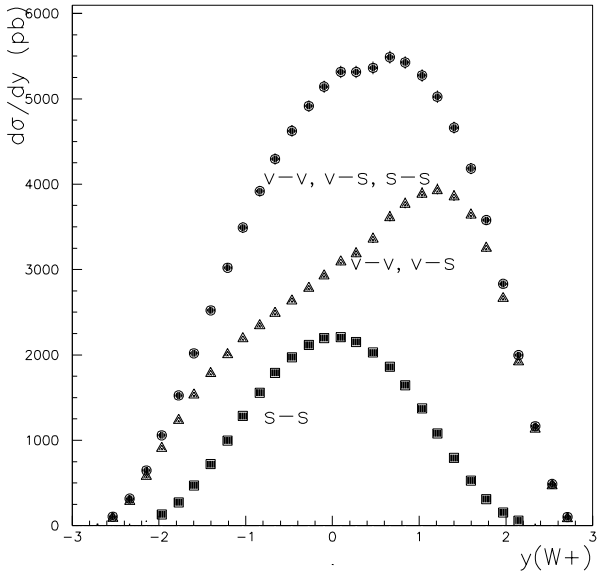

Figure 6.3: Rapidity distribution of the W^+ boson. Round symbols give the total differential cross section. Triangles give the contribution from valence-valence and valence-sea quarks. Squares give the contribution from sea-sea quarks.

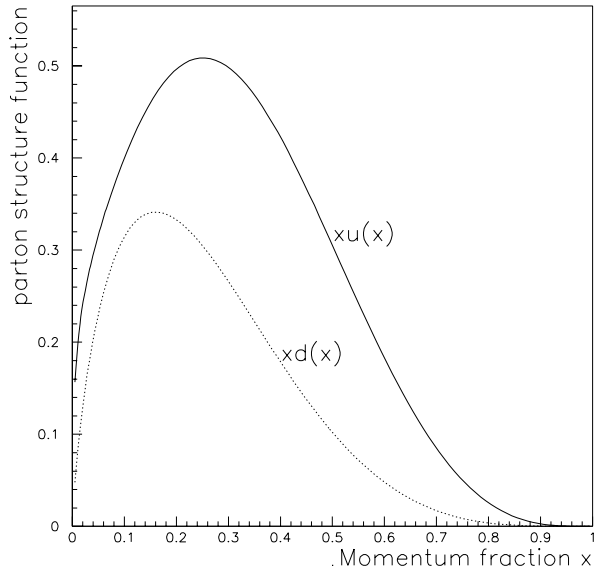

Figure 6.4: u and d quark structure functions.

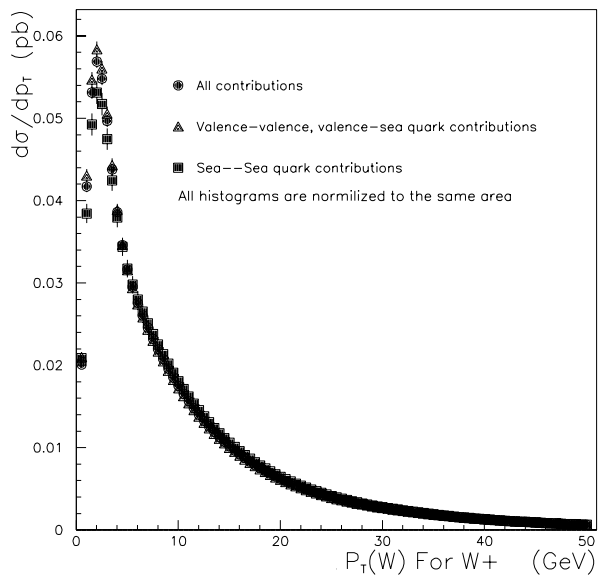

Figure 6.5: The transverse momentum distribution of the W^+.

A relativistic Breit-Wigner shape is used to model the W resonance line shape. The formula used is given in Eq. 6.4.

$$f(m) = \frac{m^2}{(m^2 - M_W^2)^2 + \frac{m^4 \Gamma_W^2}{M_W^2}} \tag{6.4}$$

where M_W and , $_W$ are the mass and width of the W boson. The parton luminosity change over the Breit-Wigner resonance region is modeled by an exponential decay factor, $e^{-\beta m}$, with $\beta = 0.015$.

6.2 Fast Monte Carlo Detector Simulation

After a W^+ is generated with a given mass and momentum, it is allowed to decay to a positron and a neutrino with the angular distribution described in section 6.1[8]. A Lorentz transformation then results in the kinematic quantities of the decay positron and the neutrino in the laboratory frame. A fast detector simulation follows. The electron P_T, the recoil of the W, and the underlying event from the spectator quarks

in the $\overline{p}p$ collision are modeled separately in the fast Monte Carlo simulation.

6.2.1 Electron Energy Resolution

The electron energy resolution was studied in the DØ test beam. For the central calorimeter, the electron energy resolution is described well by the equation:

$$\frac{\sigma_e}{E} = \sqrt{\mathcal{C}^2 + (\frac{\mathcal{S}}{\sqrt{E}})^2 + (\frac{\mathcal{N}}{E})^2} \tag{6.5}$$

which includes contributions from sampling fluctuations, electronic and uranium noise, and a constant term described by the parameter $\mathcal{C}$. However, different values of $\mathcal{S}$, ranging from 13% to 17%, are required to describe the resolution in different η regions. We need a better way to describe the electron energy resolution in the whole central calorimeter.

According to [32], the energy resolution for a sampling calorimeter is:

$$\frac{\sigma_e}{E} = \frac{1}{\sqrt{N}} = 3.2\% \sqrt{\frac{E_C}{F(\xi)}} \cdot \sqrt{\frac{t}{E(GeV)}} \tag{6.6}$$

where E_C is the critical energy, $E_C \simeq 550/Z\,(MeV)$, with Z the atomic number of the material. The factor $F(\xi)$ takes into account the shortening of the track length due to the cutoff energy. E is the energy of the electron, $t = d/X_0$ is the thickness of the calorimeter in units of the radiation length, X_0. We can see that the electron energy resolution depends on the thickness of the uranium plate. Since all the uranium plates in the central calorimeter have equal thickness, the sampling term in the expression for the electron energy resolution must depend on the angle of incidence. The effective thickness of the uranium plate varies with the incident angle θ: $d = d_0/\sin\theta$ where d_0 is the thickness of uranium plate itself. Then we may rewrite Eq. 6.6:

$$\frac{\sigma_e}{E} = 3.2\% \sqrt{\frac{E_C}{F(\xi)}} \cdot \sqrt{\frac{t}{E(GeV) \cdot \sin\theta}} \tag{6.7}$$

With the conventional definition of P_T, $P_T = E \cdot \sin\theta$, we obtain a formula which should describe the electron energy resolution in the central calorimeter with a sampling term independent of η. (The noise term also depends on eta but this doesn't matter much.)

$$\frac{\sigma_e}{E} = \sqrt{\mathcal{C}^2 + (\frac{\mathcal{S}'}{\sqrt{P_T}})^2 + (\frac{\mathcal{N}}{E})^2} \tag{6.8}$$

We shall examine both test beam data and Monte Carlo simulations of the test beam data to see if it works. Table 6.1[33] shows the electron energy resolution sampling term $\mathcal{S}$ at three different $\eta's$ obtained from Monte Carlo data with electron energies between 10 GeV and 150 GeV. The resolution varies from 13% to 17% from $\eta = 0.05$, normal incidence, to $\eta = 1.05$, a 60° incident angle. The term $\mathcal{S}'$ comes from using Eq.6.8. The variation is much smaller, only 0.5%. It is clear that Eq.6.8 describes the Monte Carlo data better than Eq.6.5 does for different incident angles with a single sampling term.

Table 6.2[34] gives the results of measurements made in the test beam. Again, different sampling terms are required in Eq. 6.5 to describe the data at different η, i.e. different incident angles. However, only one sampling term is needed for the entire central calorimeter if Eq.6.8 is used. We conclude that Eq.6.8 is the best formula to describe the electron energy resolution in the central calorimeter. The following choices are made for the coefficients of the constant, sampling, and noise terms.

$$\mathcal{C} = 0.003,\ \mathcal{S}' = 0.13\sqrt{GeV},\ \mathcal{N} = 0.38\ GeV \tag{6.9}$$

A similar argument holds for the end calorimeters. However, the variation in incident angles for trajectories pointing to the end calorimeters is small. There is no observable change in the sampling term in the test beam data. Eq.6.5 is used with the following parameters.

$$\mathcal{C} = 0.003,\ \mathcal{S}' = 0.157\sqrt{GeV},\ \mathcal{N} = 0.4\ GeV \tag{6.10}$$

Test Beam Load II Monte Carlo Data

η	$\mathcal{C}$	$\mathcal{N}$	$\mathcal{S}$	$\mathcal{S}'$
0.05	0.005	0.0	0.128	0.128
0.45	0.005	0.0	0.131	0.130
1.05	0.005	0.0	0.168	0.133

Table 6.1: Comparison of the sampling constants $\mathcal{S}$ and $\mathcal{S}'$ in the electron energy resolution (Monte Carlo).

Test Beam Load II Data

		Sampling fraction set 5			Sampling fraction set 1		
η	$\mathcal{N}$(fixed)	$\mathcal{C}$	$\mathcal{S}$	$\mathcal{S}'$	$\mathcal{C}$	$\mathcal{S}$	$\mathcal{S}'$
0.05	0.43	0.003	0.134	0.134	0.003	0.131	0.131
0.45	0.43	0.005	0.129	0.123	0.003	0.136	0.129
1.05	0.27	0.000	0.165	0.130	0.000	0.175	0.138

Table 6.2: Comparison of the sampling constants $\mathcal{S}$ and $\mathcal{S}'$ in the electron energy resolution (test beam data). The comparison is made for two choices of the sampling fractions. See text for reference.

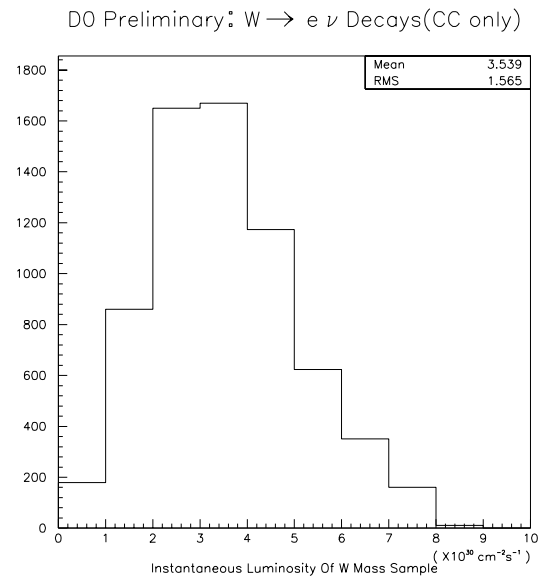

Figure 6.6: Distribution in instantaneous luminosity at which W events were acquired.

After adopting the electron energy resolution parameterization from the test beam data, we used the $Z \rightarrow ee$ invariant mass spectrum observed in the collider data to extract the constant term while keeping the same sampling term and noise term as in the test beam. Fitting to the collider Z events gives $\mathcal{C} = (1.0 \pm 0.8)\%$. The 0.8% uncertainty in the electron energy resolution contributes to the systematic error in the W mass.

6.2.2 Hadronic Response Of P_T^W Recoil

The recoil of the W, with P_T^W and y_W obtained from the Arnold-Kauffman calculation, is treated as a jet and smeared according to the DØ jet energy resolution.

The underlying event is modeled using real collider minimum bias events. Fig. 6.6 shows the distribution in instantaneous luminosity at which the events were acquired in the W analysis. The data were acquired over almost a decade in instantaneous luminosity. Minimum bias events for the underlying event are chosen at a scaled

value of the luminosity that makes the multiple interaction rate in the Monte Carlo generated W events the same as in the W data sample. From [35], we know the expected average number of interactions in a W event $\overline{n}_W$ is given by Eq. 6.11,

$$\overline{n}_W = 1 + \sigma L_W t, \tag{6.11}$$

where σ is the total inelastic scattering cross section integrated over the DØ acceptance, i.e. $\sigma = 43\,mb$. L_W is the instantaneous luminosity at which the W event is produced, and t is the time between bunch crossing time, i.e. $t = 3.5\,\mu s$.

For the minimum bias trigger, the average number of events per crossing , $\overline{n}_{min}$, given that there is at least one, is:

$$\overline{n}_{min} = \frac{\sum n f_{\overline{n}}(n)}{\sum_{n=1}^{\infty} f_{\overline{n}}} = \frac{\overline{n}}{1 - f_{\overline{n}}(0)} \tag{6.12}$$

where $\overline{n}$ is the average number of event per crossing and $f_{\overline{n}}(0)$ is the Poisson probability function $f_{\overline{n}}(n) = \overline{n}^n e^{-\overline{n}}/n!$ for $n = 0$. Substituting $\overline{n} = \sigma L_{min} t$ in 6.12 and requiring $\overline{n}_W = \overline{n}_{min}$, we obtain:

$$1 + \sigma L_W t = \frac{\sigma L_{min} t}{1 - e^{-\sigma L_{min} t}} \tag{6.13}$$

For a given W event occurring at instantaneous luminosity L_W, we can solve for the required instantaneous L_{min} at which to pick the minimum bias event. This equation can be easily solved graphically. For the distribution in instantaneous luminosity of the W mass sample, shown in Fig. 6.6, we can find a matching instantaneous luminosity distribution of minimum bias events and use it to select minimum bias events in the MC model. The main vertex of the minimum bias event is used as the W event vertex. This allows matching of the MC vertex distribution with that from the beam automatically.

The energy flow in minimum bias event and that underlying the W event are compared by studying the scalar E_T as a function of pseudorapidity η. The disagreement is less than 10%. This uncertainty contributes to the uncertainty in the

W mass and is included as a systematic error. The fluctuations in the underlying event and the uncertainty in the recoil momentum shift and smear the spectrum in the transverse momentum of the W. These two effects cannot be separated in the data. The transverse momentum of the W is calculated from the missing P_T and the electron momentum, $\vec{P}_T^W = \vec{P}_T^\nu + \vec{P}_T^e$. The scale of the measured P_T^W differs from the electromagnetic scale because the missing P_T involves energy in the hadronic calorimeter. This scale is obtained by studying Z events. In a Z event, P_T^Z can be obtained in two ways: from the measurement of the transverse momenta of the two electrons, $\vec{P}_T^{ee}$, and from the recoil activity in the Z event, $-\vec{P}_T^{rec}$, which is the way P_T^W is measured in W events. Fig. 6.8 shows a schematic view of the two measurements of the $\vec{P}_T^Z$ projection onto the bi-sector of the angle between the electron $\vec{P}_T$'s, the η axis. The advantage of using the η axis is to minimize the effect of electron energy resolution. We define the difference of the two measurements as:

$$\Delta \equiv \vec{P}_T^{ee} \cdot \hat{\eta} + \vec{P}_T^{rec} \cdot \hat{\eta} \tag{6.14}$$

A linear fit to Δ as a function of $\vec{P}_T^{ee} \cdot \hat{\eta}$ relates the hadronic recoil measurement of P_T^Z to that measured from the two electrons: $P_T^{rec} = \alpha P_T^{ee}$, see Fig 6.7. The value of α found is 0.83 ± 0.06. The error has been expanded to include both the statistical error and the deviations from linearity of the fit. The effect of this uncertainty on the W mass has been calculated and included as a systematic error.

6.2.3 Trigger And $u_{||}$ Efficiencies

The threshold for the electron P_T is set at 10 GeV in the Level 1 trigger. The threshold is 20 GeV on both the electron P_T and missing P_T in the Level 2 trigger. As a result of resolution broadening, and because these triggers do not use the full information available to the offline analysis, the triggers are not fully efficient until higher energies are reached in both variables. The trigger efficiencies are modeled in the Monte Carlo simulation. The electron and missing P_T trigger efficiencies are

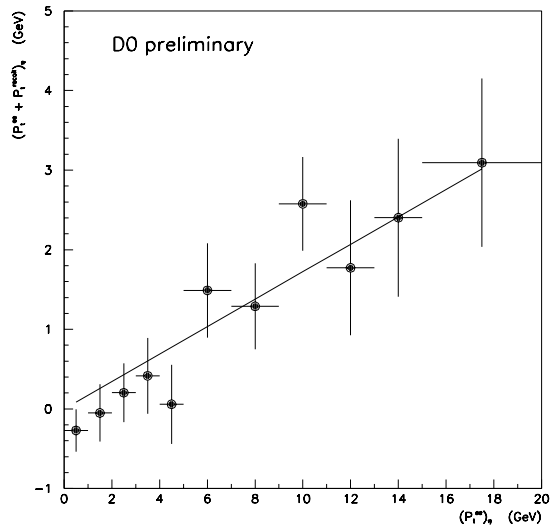

Figure 6.7: The P_T^Z obtained from the two electrons minus the P_T^Z calculated from the recoil, projected along the bisector of the angle between the two electron P_T's. Δ vs $\vec{P}_T^{ee} \cdot \hat{\eta}$. (See text for the definition of Δ.)

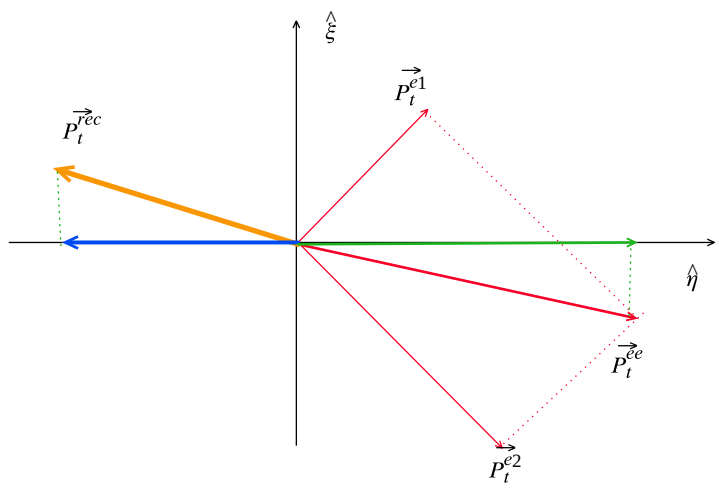

Figure 6.8: Vector diagram showing the projections of the ee and recoil measurements of P_T^Z onto the bi-sector of the angle between the two electron P_T's.

studied independently as a function of offline electron and missing P_T respectively. These trigger turn-on curves are used in the Monte Carlo simulation.

Figs. 6.9 (a) and (b) show the electron trigger turn-on curves. They are obtained by comparing to the number of events obtained with a lower threshold:

$$\epsilon(P_T) = \frac{N(P_T, P_H)}{N(P_T, P_L)}, \tag{6.15}$$

where $\epsilon(P_T)$ is the efficiency at P_T and P_H and P_L are the high and low trigger thresholds. A third of the data were taken without the z vertex information in the trigger, Fig. 6.9(a). Two thirds of the data were taken with the z vertex measured by the Level 0 detectors (called the Slow_Z vertex in DØ jargon.) The efficiency for these data are shown in Fig. 6.9(b). Similar trigger turn-on curves are shown in Figs. 6.10 for missing P_T. In general, the use of the z vertex information improves the resolution in P_T (or missing P_T) and full efficiency is reached more rapidly, at a lower value of P_T. Approximations to error functions are used to fit the curves. The trigger is about 95% efficient for electrons with $P_T = 25$ GeV and 90% efficient for missing P_T of 25 GeV.

A measure of event selection biases— electron shape cuts, isolation cuts, etc.— can be obtained by studying the projection of the momentum recoiling against the W along the electron P_T, called $u_{||}$ in Fig. 6.11. Electron selection criteria can bias the data against events in which the hadronic recoil against the W is large, and in the same direction as the electron. The projection $u_{||}$ is plotted vs. P_T^W and compared to the Monte Carlo in Fig. 6.12. The efficiency used in Fig. 6.12(b) was obtained independently by tightening the isolation cut and H-matrix χ^2 cut and observing the number of events lost as a function of $u_{||}$.

Various calorimeter and tracking chamber fiducial cuts are also implemented in the fast Monte Carlo simulation. It is important to simulate those cuts correctly because they affect the electron η distribution which affects the shape of the transverse mass spectrum, and the W mass.

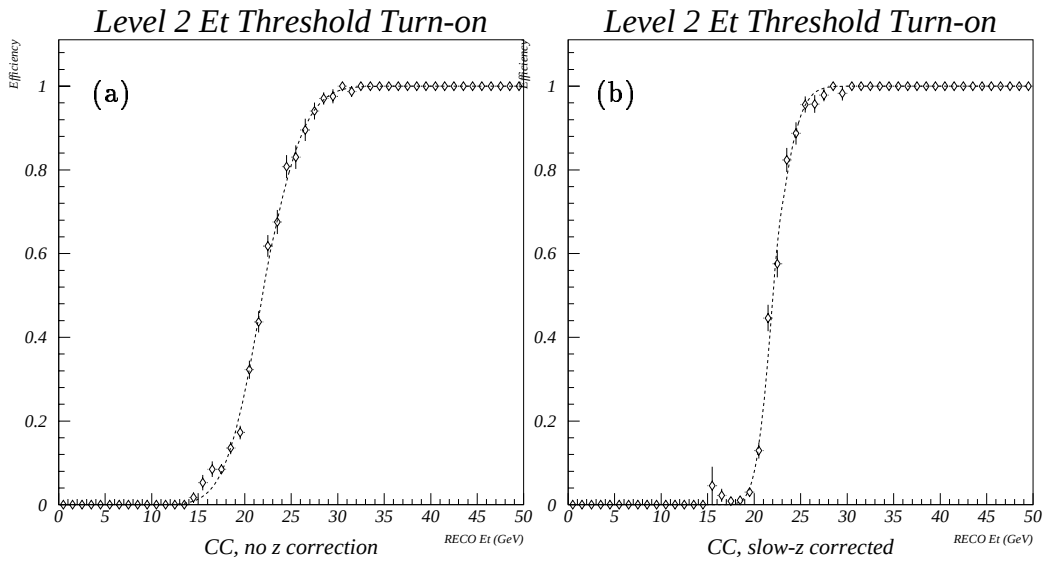

Figure 6.9: Electron trigger turn-on curves. (a) Turn-on curve measured without z vertex information. (b) Turn-on curve with z vertex measured by Level 0 trigger(called Slow Z vertex).

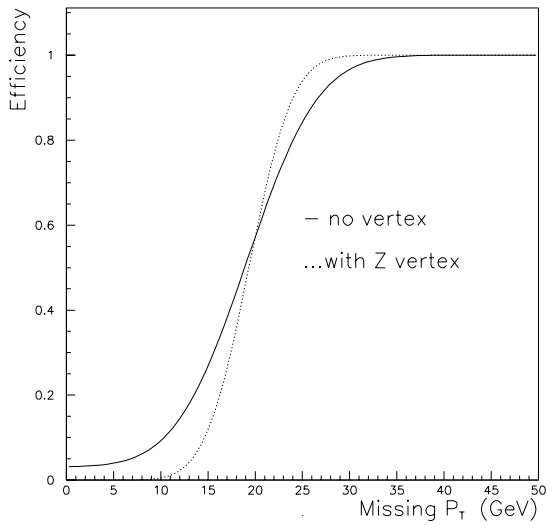

Figure 6.10: Missing P_T trigger turn-on curves. Solid line: Turn-on curve measured without z vertex information. Dotted line: Turn-on curve with z vertex measured by Level 0.

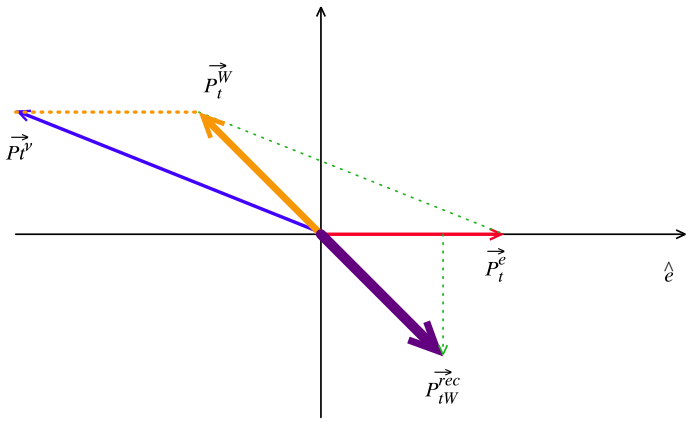

Figure 6.11: $u_{||}$ is the projection of the momentum recoiling against the W along the electron direction (in the transverse plain).

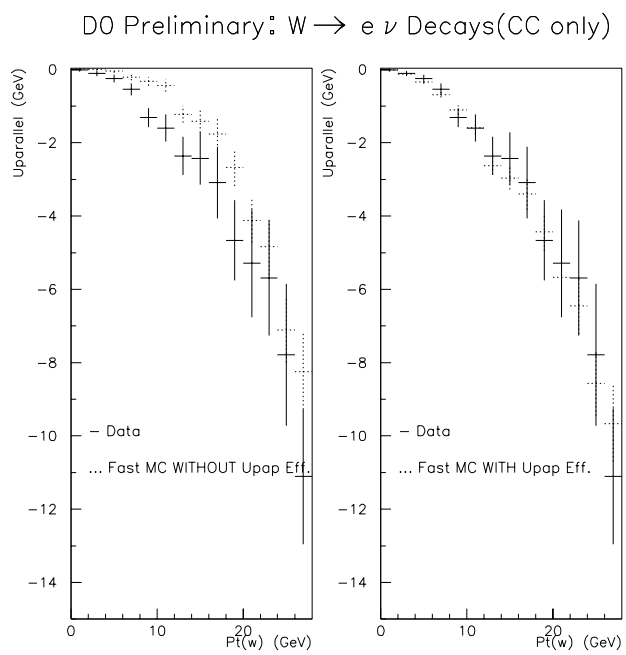

Figure 6.12: (a) $u_{||}$ vs P_T^W without $u_{||}$ efficiency in the Monte Carlo. (b) $u_{||}$ vs P_T^W with $u_{||}$ efficiency in the Monte Carlo.

6.2.4 $W \longrightarrow \tau\nu \longrightarrow e\nu\nu$ Decay Effect

A W_+ can decay to τ^+ and ν_τ. The branching ratio is the same as the W^+ decaying to a positron and a neutrino. The τ^+ can decay to a positron and two neutrinos with a 17% branching ratio. This decay channel gives a high P_T positron and large missing P_T, as in the decay of a W_+ to a positron and neutrino.(see section 4.4 in Chapter 4.) We generate this decay and follow it in the fast detector simulation. The fraction that survives all the W mass selection cuts are kept in the fast MC to simulate this effect in the data.(The same procedure is followed for W^-.)

6.3 Comparisons Between Fast MC And Data, And Mass Fitting Procedure

The W mass is extracted from a comparison of the experimental distributions to those obtained from the Monte Carlo simulation with the W mass as a free parameter. In principle, electron P_T, missing P_T and transverse mass can all be used to extract the W mass.

The transverse mass is defined in the plane transverse to the $\overline{p}p$ beam in a manner analogous to the definition of the invariant mass.

$$m_T^2(W) = (P_T^e + P_T^\nu)^2 - (\vec{P}_T^e + \vec{P}_T^\nu)^2 \tag{6.16}$$

$$= 2P_T^e P_T^\nu (1 - \cos\phi_{e\nu}) \tag{6.17}$$

where P_T^e and P_T^ν are the electron and neutrino transverse momenta, and $\phi_{e\nu}$ is the angle between the electron and the neutrino in the transverse plane. The neutrino P_T comes from the missing P_T measurement, which involves all the calorimeter cells. It generally suffers from poor resolution and detector biases. Among the three quantities, the electron P_T is the best measured. But W's are not produced at rest. The transverse momentum of the electron is sensitive to P_T^W. The spectrum

in P_T^W can be modeled theoretically but only with large uncertainty. On the other hand, transverse motion of the W shifts the transverse mass only by terms of order $P_T^{2W}/(m_W^2 + P_W^2)$[13]. Generally, smaller systematic errors are expected in fitting the transverse mass distribution than fitting either the electron or neutrino P_T distributions. The electron and neutrino P_T distributions serve as good cross checks.

The fast simulation generates transverse mass spectra as a function of the input W mass. These spectra are compared with data using a maximum likelihood method. Fig. 6.13(a) shows the best fit Monte Carlo transverse mass spectrum overlapped with the data.

Fig. 6.14, Figs. 6.15(a), (b), and Figs. 6.16(a),(b) show the comparison between data and Monte Carlo for the spectra in W, electron, and neutrino transverse momenta, and also for the distributions in the variables $u_{||}$ and $u_{\perp}$. In these comparisons, the W mass obtained from the fit to the transverse mass was used in the Monte Carlo simulation. Data and Monte Carlo agree very well. The W mass is obtained from a fit with a fixed W width of 2.12 GeV. The W mass scaled by the ratio of the Z mass measured at LEP to the Z mass measured in this experiment, is

$$M_w = (79.86 \pm 0.16(stat))\, GeV \tag{6.18}$$

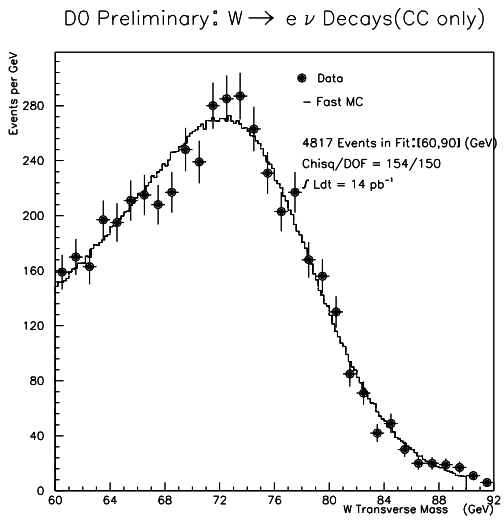

Figure 6.13: Transverse mass spectrum compared to Monte Carlo simulation. The chi-squared was calculated by comparing data and Monte Carlo in 200 MeV bins in transverse mass between 60 GeV and 90 GeV.

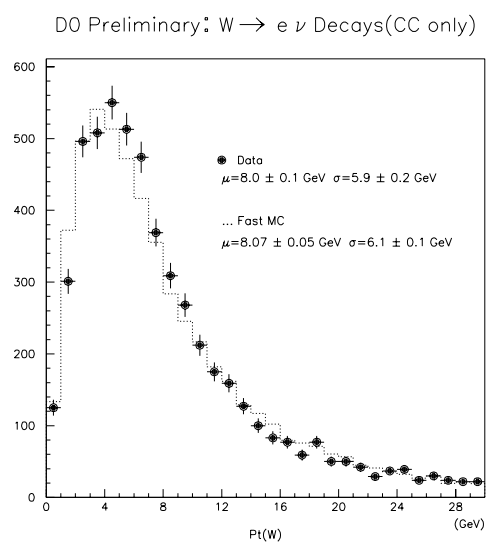

Figure 6.14: Spectrum in P_T^W compared to the Monte Carlo simulation.

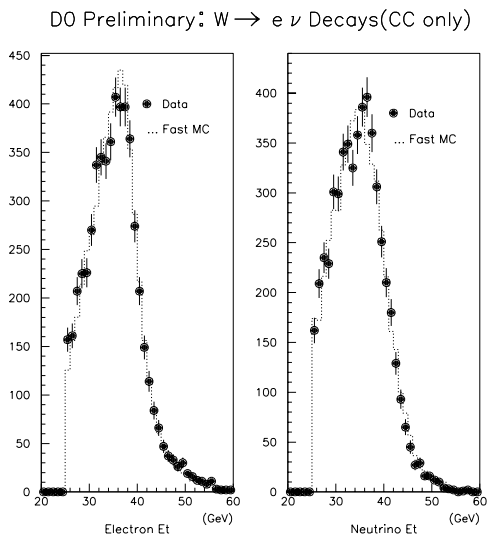

Figure 6.15: The overlap of Monte Carlo simulation(curve) onto data distribution (dots with error bars). (a) Electron P_T. (b) neutrino P_T.

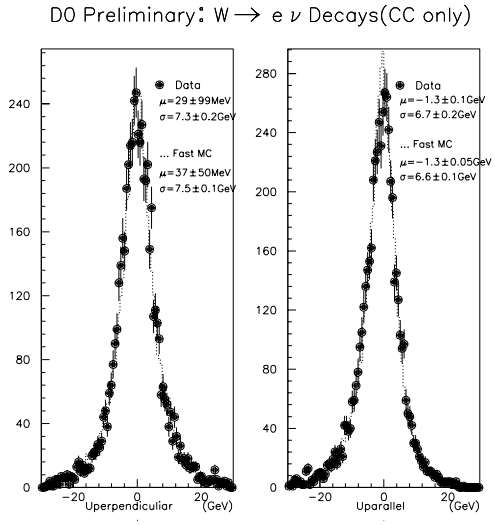

Figure 6.16: The overlap of Monte Carlo simulation(curve) onto data distribution (dots with error bars). (a) $u_\perp$. (b) $u_{||}$.

Chapter 7

Systematic And Energy Scale Uncertainties

In Chapter 6, we obtained the W mass and the statistical error in the W mass by fitting to the W transverse mass shape. We now examine all the important systematic uncertainties, and obtain the error in the W mass from the uncertainty in the energy scale that remains after normalizing our measured Z mass to the Z mass measured at LEP.

7.1 Systematic Uncertainties

There are many theoretical and experimental issues which must be considered to obtain the W mass at a level of accuracy of 100 MeV. The systematic error in the W mass is the change in the W mass that results when the uncertain factor is varied by one standard deviation from its nominal value. The important items are discussed below.

7.1.1 Trigger Efficiencies

In the Level 2 trigger, a 20 GeV threshold is imposed on both the electron P_T and the missing P_T. Figs. 6.9 (a) and (b) show the turn-on curves for electron triggers. Fig. 6.10 shows the missing P_T trigger turn-on curves. The errors on the fitted parameters are very small. There is no noticeable effect on the W mass when the fitted parameters are varied by one standard deviation. The trigger turn-on curves without (or with) z vertex were used separately, not weighted according to the data, to look at the effect on the W mass. The variation from this approximation is larger than that caused by possible deviations from the form described by the analytical formula. The change in the W mass is 20 MeV.

7.1.2 Electron Energy Resolution

Section 6.2.1 in Chapter 6 describes the parameterization of electron energy resolution and constrains the constant term to be $\mathcal{C} = 1.0 \pm 0.8\,\%$. The 0.8% uncertainty is varied in the MC model and results in a change of 70 MeV in the W mass.

7.1.3 Neutrino P_T Scale And Resolution

It is easy to understand how the underlying event might affect the neutrino P_T resolution. Here we shall show that it also affects the neutrino P_T scale.

Fig. 7.1 shows a schematic view of the measurable quantities in solid lines on the transverse plan of a W event. $\vec{P_T^{rec}}$ denotes the recoil activities against the W. $\vec{u}$ denotes the underlying event from the debris of the W production, i.e. spectator quarks. $\vec{P_T^e}$ represents the electron P_T from the W decay. Generally $\vec{P_T^{rec}}$ and $\vec{u}$ cannot be separated from each other in the actual measurement. The missing transverse momentum is defined by Eq. 7.1:

$$\vec{\not{P}_T} \equiv -(vector\,sum\,of\,all\,measured\,transverse\,momentum) \equiv -\sum \vec{P_T^i} \qquad (7.1)$$

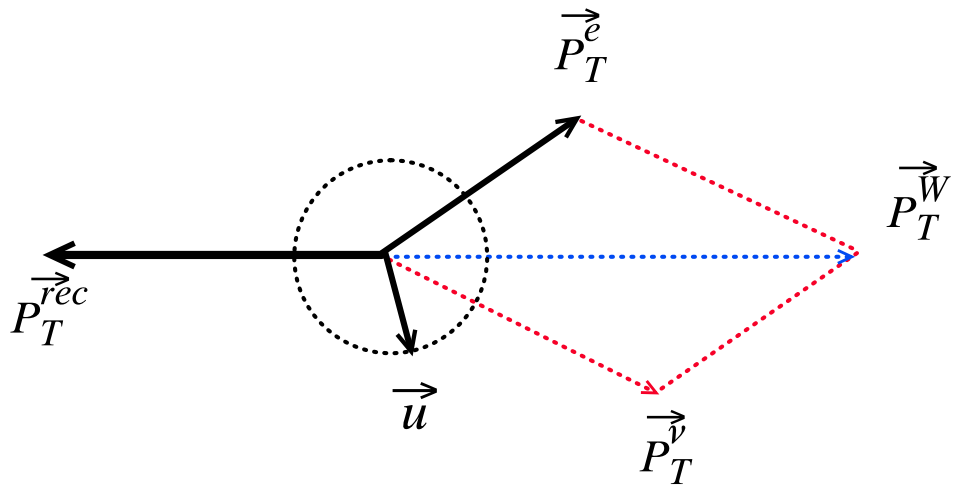

Figure 7.1: A typical W event in the transverse plane: solid lines indicate the measured quantities. See text for the meaning of each item.

For the W event shown in Fig. 7.1, the missing P_T is given by Eq. 7.2:

$$\vec{\not{P}}_T = -(\vec{P_T^e} + \vec{P_T^{rec}} + \vec{u}), \tag{7.2}$$

and the neutrino P_T is

$$\vec{P_T^\nu} = \vec{P_T^W} - \vec{P_T^e} = -\vec{P_T^{rec}} - \vec{P_T^e}. \tag{7.3}$$

So, we have the relationship between the missing transverse momentum and the neutrino P_T from Eq. 7.2 and Eq. 7.3:

$$\vec{\not{P}}_T = \vec{P_T^\nu} - \vec{u}. \tag{7.4}$$

Since the underlying event $\vec{u}$ is randomly distributed with regard to the direction of the neutrino P_T, on average the direction of the missing P_T will be the same as that of the neutrino from W decay. But the average amplitude of the missing P_T is not necessarily the same as that from the neutrino P_T.

$$\not{P}_T = \sqrt{(P_T^\nu)^2 + u^2 - 2P_T^\nu u \cos\phi_{u\nu}} \tag{7.5}$$

$$\simeq P_T^\nu + \frac{1}{2}\cdot\frac{u^2}{P_T^\nu} - u\cos\phi_{u\nu} - \frac{1}{2}\frac{u^2}{P_T^\nu}\cdot\cos^2\phi_{u\nu}, \quad P_T^\nu >> u \tag{7.6}$$

$$\tag{7.7}$$

where $\phi_{u\nu}$ is the angle between the neutrino P_T and the underlying event vector u. Setting $< \cos\phi_{u\nu} >= 0$ and $< \cos^2\phi_{u\nu} >= 0.5$, we get:

$$<\not{P}_T > \simeq < P_T^\nu > + \frac{1}{4} \cdot \frac{< u^2 >}{< P_T^\nu >}, \;\; P_T^\nu >> u. \tag{7.8}$$

The requirement $P_T^\nu >> u$ is generally true. So the average missing P_T is generally larger than the the neutrino P_T. For typical values of $< u^2 >= 30\,GeV^2$ and $< P_T^\nu >= 35GeV$, $<\not{P}_T > - < P_T^\nu > \simeq 215\,MeV$, a significant shift. Therefore, the understanding of the underlying event will directly affect our neutrino P_T scale. We use minimum bias events from collider data to simulate the W underlying event. This approach was checked by comparing, as a function of pseudorapidity η, the mean scalar E_T in minimum bias events and W events. In the W events, the scalar E_T was studied as a function of P_T^W and extrapolated to $P_T^W = 0$ to estimate the contribution from the underlying event. The scalar E_T distributions in W and minimum bias events agree to within 10%. This uncertainty is varied in the MC model and results in a change of 130 MeV in the W mass.

7.1.4 Energy Underlying An Electron

The debris in the proton and anti-proton collisions that produce a W can also deposit energy in the same calorimeter cells as the decay electron from the W. This causes the measured energy of the electron to be too large. This effect is studied with W events and minimum bias events. Eq. 7.9 gives the parameterization of the energy underlying the electron as a function of detector pseudorapidity η.

$$\Delta E = 0.091 + 0.022\eta^2 + 0.025\eta^4\,(GeV) \tag{7.9}$$

The uncertainty is 20 – 40 MeV. The electron energies are corrected downward by this amount. Because of the energy underlying the electron, both the W and Z masses are shifted. The shifts are already incorporated in the W and Z mass values

given by Eq. 8.2 and Eq. 5.23 respectively. The uncertainty on the shifts after we take the ratio of W to Z mass and scale it to the LEP Z value is 50 MeV.

7.1.5 Hadronic To EM Scale

Section 6.2.2 of Chapter 6 described the method of normalizing the response of P_T^W, which is mostly hadronic energy, to the EM scale and gave $P_T^{rec} = \alpha P_T^{ee}$ with $\alpha = 0.83 \pm 0.06$. A change of 0.06 in α in the MC model gives a change of 80 MeV in the W mass.

7.1.6 QCD Background

The QCD background is determined directly from data to be $2 \pm 1\%$ in section 4.4 of Chapter 4. After all the W mass selection cuts are applied, there are only a handful of events left. It is hard to determine the transverse mass shape of the QCD background. Two assumptions for the shape of the background were tried to study the variation of the W mass. The first assumes the transverse mass shape of the QCD background to be exponentially falling between 50 GeV and 100 GeV. This assumption is put into the MC model and normalized to the values stated above. There is no observable effect on the measured W mass. The second assumes a background flat in transverse mass. With the background level and uncertainty stated above, the W mass changes by 30 MeV.

7.1.7 Structure Functions

This study varies the structure functions used in the MC generation. Most of the popular structure functions are tried. The variation in the W mass is 70 MeV. Future studies will discriminate 'good' structure functions from 'bad' ones according to their agreement with the experimental data. This will reduce the systematic error from this source.

7.1.8 Uncertainty On The W Width

The W mass obtained from the fit was at a fixed value of the W width, , $= 2.12\,GeV$. The width was varied by ± 0.11 GeV, the current error in the width of the W. This variation changed the W mass by ± 20 MeV.

7.1.9 Fitting Error

The error due to uncertainties in the fitting procedure is obtained by varying the fitting window in W transverse mass. It is discussed in detail in section 8.2.1 of Chapter 8. A 30 MeV change is seen.

7.1.10 Summary

Table 7.1 summarizes various contributions to the systematic errors. The total systematic error is 200 MeV. The effect of radiative decays is still under study.

7.2 Uncertainty On EM Energy Scale

Two methods are used to determine the energy scale error.

- **Method I :** Uses both Z and J/ψ signals to constrain the EM scale.
- **Method II:** Uses Z events alone to obtain the EM scale and offset.

Method I: We have observed $J/\psi \longrightarrow e^+e^-$ with more than 3σ significance. Fig. 7.3(a) shows the ee invariant mass spectrum in the region of the J/ψ. The measured mass is $m_{J/\psi} = (3.00 \pm 0.27)\,GeV$.

We define the scale factor α and energy offset β through the following formula:

$$E_{true} = \alpha E_{measured} + \beta \tag{7.10}$$

Source of Uncertainty	**MeV**
Trigger Efficiency	20
Resolution and neutrino P_T scale†	149
Energy underlying electron	50
$u_{\parallel}$ efficiency	10
Hadronic to EM scale	80
QCD background	30
Theoretical model uncertainty‡	86
W width	20
Fitting Error	30
Total	200

† *Resolution and neutrino P_T scale*	
Electron energy resolution	70
Neutrino P_T scale, resolution (W underlying event)	130
Jet energy resolution	20

.

.

‡ *Theoretical model uncertainty*	
Structure function	70
P_T^W spectrum	50

Table 7.1: Systematic uncertainties on the W mass measurement(DØ Preliminary)

where E_{true} stands for the true electron energy and $E_{measured}$ is the electron energy measured in the calorimeter. The invariant mass of the two electrons is:

$$m_{true} = \sqrt{2E_1^{true}E_2^{true}(1-\cos\gamma)} \tag{7.11}$$

where γ is the opening angle between the two electrons. Substituting Eq. 7.10 into Eq 7.11, we have

$$m_{true} \simeq \alpha m_{measured} + \beta f \tag{7.12}$$

where $f = 2(E_1^{measured} + E_2^{measured})/m_{measured}\sin^2(\gamma/2)$. Using the measured Z and J/ψ masses, and the average f-factors for the two decays, we find $\alpha = 1.047 \pm 0.009$, $\beta = 12 \pm 340\ MeV$. The parameters α and β are strongly correlated, as one might expect. The corresponding error in the W mass is $\delta(M_W) = 195\ MeV$.

Method II: Electrons from Z decays are not monochromatic. Electrons in the central calorimeter vary in energy from 45 GeV to 70 GeV. For Z decays with electrons back to back, i.e. $E_1 \simeq E_2 \simeq 45\ GeV$, the f factor is about 2. For Z decays with small opening angles, i.e. $E_1 \simeq E_2 \simeq 70\ GeV$, the f-factor is about 1.5. A linear fit to the measured Z mass as a function of the f-factor is shown in Fig. 7.3(b), and gives $\alpha = 1.043 \pm 0.013$, $\beta = 270 \pm 620\ MeV$. These values are consistent with those determined from the first method. Again, α and β are strongly correlated. The advantage of this method is that it fixes the electron energy scale using high energy electrons in the same energy range as those from W decays. With this method we arrive at a scale error of $\Delta(M_W) = 310\ MeV$.

We can see that both methods give offsets consistent with zero. This justifies the zero offset assumption used in Chapter 5 to derive the EM energy scale from our measured Z mass. Therefore, no correction is made on the Z mass obtained in Chapter 5. The larger uncertainty, $\Delta(M_W) = 310\,MeV$, is retained as the systematic error since we are still working on the J/ψ signal.

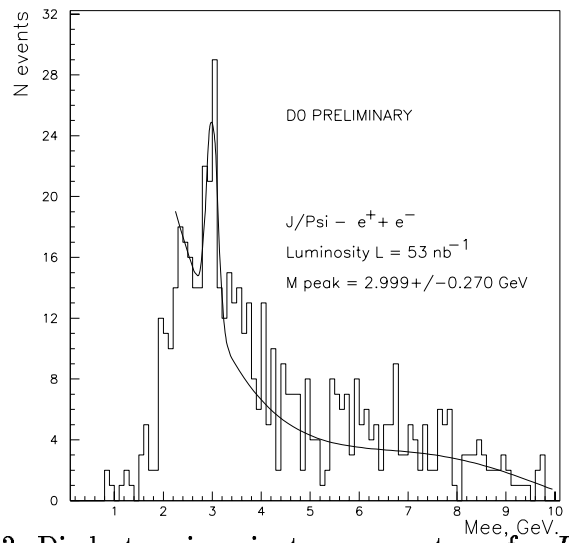

Figure 7.2: Di-electron invariant mass spectrum for J/ψ signal.

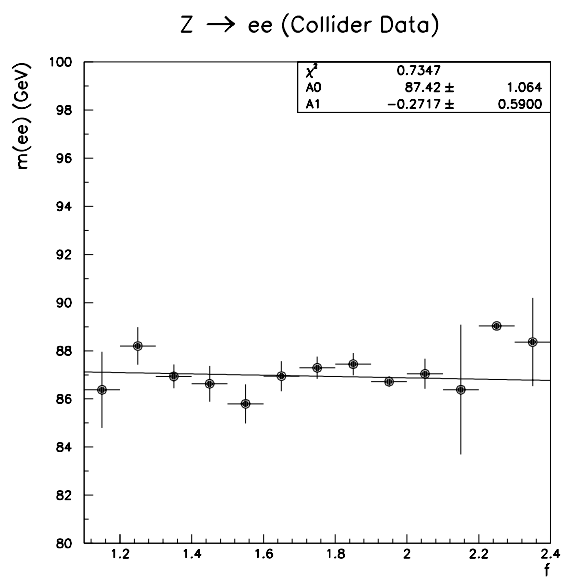

Figure 7.3: Measured Z invariant mass as a function of the f-factor with fitted curve.

Chapter 8

Results

8.1 W Mass From $W \longrightarrow e\nu$ Decay

Combining the results on the mass fitting from Chapter 6, with the systematic and scale errors found in Chapter 7, the measured W mass is:

$$M_W = 79.86 \pm 0.16(stat) \pm 0.20(syst) \pm 0.31(scale)\, GeV \tag{8.1}$$

Adding the statistical, systematic, and scale errors quadratically gives

$$M_W = 79.86 \pm 0.40\, GeV \tag{8.2}$$

The energy scale uncertainty is the larger value obtained using method II of the chapter 7. Some preliminary studies, already discussed in Chapter 7, indicate that this error can be reduced to about 200 MeV. The total error will go down to about 300 MeV.

8.2 Consistency Checks

8.2.1 Vary Fitting Window

The result presented above was obtained from a fit to the transverse mass from 60 GeV to 90 GeV. When the minimum transverse mass is changed to 50 GeV the W mass changes by 90 MeV. When it is changed to 70 GeV, the W mass changes by 140 MeV. The number of events in the fit changes when the window size is varied and to separate the statistical contribution from the real shift due to the change in the fitting range, this exercise was repeated with 40 MC samples. Each MC sample contains the same number of events as the experimental data. The mean shift observed using the 40 MC samples was 30 MeV with an rms deviation of 140 MeV. The shift observed in the data is consistent with this result. The 30 MeV shift is kept as the systematic error in the fitting procedure.

We also changed the maximum transverse mass to 92 and 94 GeV. The W mass changes is less than 20 MeV. The same changes applied to the 40 MC sample gives a mean shift of 10 MeV with an rms deviation of 20 MeV.

8.2.2 Select Single Vertex W Events:

We require only one vertex be found by the central tracking system. This reduces the event sample by 23%. The W mass obtained from this sample is $79.84 \pm 0.18\ GeV$.

8.2.3 Vary The Electron Selection Cuts:

Besides the event selection cuts discussed earlier, we require further that (i) there is only one track in the electron finding road and (ii) the ionization loss in the central tracking system is less than twice that expected from a minimum ionizing particle. The event sample is reduced by 22%. An independent study indicates that the QCD background is reduced by a factor of two. The fit to this sample gives:

$M_W = 79.89 \pm 0.18\, GeV$. This result is consistent with the QCD background study.

Chapter 9

Conclusions

There have been, up to now, six measurements of the W mass. They all come from the observation of W's decaying to leptons. The measured masses are listed in Table 9.1, along with the errors reported by each experiment.

We can combine the measurements to obtain a world average W mass and the error associated with it. Since correlations exist among different experiments and also, for the CDF experiment, between the electron and muon decay mode results, it is quite complicated to properly combine the errors. We proceed by first combining the results of the CDF electron and muon channel measurements, taking the

Experiment	Mode	M_W	Stat	Syst	scale	total
CDF(1991) [36]	e	79.91	0.35	0.24	0.19	0.46
	μ	79.90	0.53	0.32	0.08	0.62
UA2(1992) [37]	e	80.37	0.22	0.17	0.25	0.37
DØ (1993) [38]	e	79.86	0.16	0.20	0.31	0.40
CDF(1994) [39]	e	80.47	0.15	0.21	0.13	0.29
	μ	80.29	0.20	0.22	0.06	0.30

Table 9.1: A summary of all W mass measurements (unit in GeV).

correlations within the same data run, such as that due to the energy scale error, into account. We then combine these results with the other experiments. We shall assume that the only error common to experiments using different detectors is the uncertainty resulting from imprecise knowledge of the structure functions. It is assumed that there is no correlation between the CDF 1991 and 1994 results, aside from that due to the structure functions. The uncertainty from the structure functions ranges from 60 to 100 MeV, as reported by the various experiments. We take it to be 80 MeV.

9.0.4 Method

We consider, for simplicity, the case of combining two experiments. It can be generalized easily to many dimensions.

Let us assume that we have two measurements X_1 and X_2 of a quantity whose true value is X. The error matrix $\mathbf{M}$ is:

$$\mathbf{M} = \begin{pmatrix} \sigma_1^2 & \sigma_{12} \\ \sigma_{21} & \sigma_2^2 \end{pmatrix} \tag{9.1}$$

Where σ_1, σ_2 are the errors on the measurement X_1, X_2 respectively and $\sigma_{12} = \sigma_{21} = cov(X_1, X_2)$ is the covariance of the two measurements. The inverse matrix $\mathbf{M^{-1}}$ is:

$$\mathbf{M^{-1}} = \frac{1}{1-\rho^2} \begin{pmatrix} \frac{1}{\sigma_1^2} & -\frac{\rho}{\sigma_1\sigma_2} \\ -\frac{\rho}{\sigma_1\sigma_2} & \frac{1}{\sigma_2^2} \end{pmatrix} \tag{9.2}$$

where $\rho = cov(X_1, X_2)/\sigma_1\sigma_2$ is known as the correlation coefficient. We shall denote $\mathbf{M^{-1}}$ as in Eq. 9.3 for convenience.

$$\mathbf{M^{-1}} = \begin{pmatrix} a_{11} & a_{12} \\ a_{12} & a_{22} \end{pmatrix} \tag{9.3}$$

The χ^2 of the two measurements can be constructed as:

$$\chi^2 = (X - X_1)^2 a_{11} + 2(X - X_1)(X - X_2)a_{12} + (X - X_2)^2 a_{22} \tag{9.4}$$

The derivative of the χ^2 with respect to X is:

$$\frac{\partial \chi^2}{\partial X} = 2(X - X_1)a_{11} + 2a_{12}(X - X_2) + 2a_{12}(X - X_2) + 2a_{22}(X - X_2) \tag{9.5}$$

Setting $\partial\chi^2/\partial X = 0$, we find the formula, Eq. 9.6, for the best estimate of X.

$$\overline{X} = \frac{X_1 a_{11} + X_1 a_{12} + X_2 a_{12} + X_2 a_{22}}{a_{11} + 2a_{12} + a_{22}} \tag{9.6}$$

Plugging a_{11}, a_{12}, and a_{22} into Eq. 9.6, we get:

$$\overline{X} = \frac{X_1(\frac{1}{\sigma_1^2} - \frac{cov(X_1,X_2)}{\sigma_1^2\sigma_2^2}) + X_2(\frac{1}{\sigma_2^2} - \frac{cov(X_1,X_2)}{\sigma_1^2\sigma_2^2})}{\frac{1}{\sigma_1^2} - 2\frac{cov(X_1,X_2)}{\sigma_1^2\sigma_2^2} + \frac{1}{\sigma_2^2}} \tag{9.7}$$

The error in $\overline{X}$ is obtained from Eq. 9.8[43]:

$$\overline{\Delta X^2} = \tilde{D}\mathbf{M}D \tag{9.8}$$

where D is the derivative vector calculated from the transformation, Eq. 9.6, and $\tilde{D}$ its transpose.

$$D = \begin{pmatrix} \partial X/\partial X_1 \\ \partial X/\partial X_2 \end{pmatrix} \tag{9.9}$$

$$= \begin{pmatrix} \frac{a_{11}+a_{12}}{a_{11}+2a_{12}+a_{22}} \\ \\ \frac{a_{22}+a_{12}}{a_{11}+2a_{12}+a_{22}} \end{pmatrix} \tag{9.10}$$

Once we know the covariance between the two measurements, we can easily combine the measurements using Eq. 9.7. The associated error is obtained from Eq. 9.8.

The issue is how to calculate the covariance of the two measurements. We shall assume that the two measurements are positively correlated and the covariance of the two experiments is the common error squared. We can justify this in following situation.

Suppose we have two measurements, X_1 and X_2. Their errors are σ_1 and σ_2 respectively. Assume the common error σ_c is the same as σ_2. This implies that

$\sigma_1 > \sigma_2$. Common sense tells us that we should just use the second measurement, X_2, as the combined result, since it contains no additional error of any kind. If we impose this condition on Eq. 9.7, we require the coefficient of X_1 to be zero:

$$\frac{1}{\sigma_1^2} - \frac{cov(X_1, X_2)}{\sigma_1^2 \sigma_2^2} = 0 \tag{9.11}$$

We find

$$cov(X_1, X_2) = \sigma_c^2 \tag{9.12}$$

Substituting this in Eq. 9.7, we find a simple expression for $\overline{X}$:

$$\overline{X} = \frac{X_1(\sigma_2^2 - \sigma_c^2) + X_2(\sigma_1^2 - \sigma_c^2)}{\sigma_1^2 + \sigma_2^2 - 2\sigma_c^2} \tag{9.13}$$

The result is to weight the experiments with the uncorrelated errors. We shall use Eq. 9.13 and Eq. 9.8 to evaluate the world average W mass and its error in the following sections.

9.0.5 The World Average W Mass

Combining the Electron And Muon Channels From the CDF 1991 Experiment.

We use

$$M_e = 79.91\, GeV \quad M_\mu = 79.90\, GeV \tag{9.14}$$

$$\sigma_e = 0.465 \;\; GeV \quad \sigma_\mu = 0.620\, GeV \quad \sigma_c = 0.17\, GeV \tag{9.15}$$

in Eq. 9.13 and Eq. 9.8. We find

$$M_{cdf1991} = 79.91 \pm 0.39\, GeV, \tag{9.16}$$

the result presented by CDF in their publication[36].

Combining the Electron And Muon Channels From the CDF 1994 Experiment.

Use

$$M_e = 80.47\,GeV \quad M_\mu = 80.29\,GeV \tag{9.17}$$

$$\sigma_e = 0.29\,GeV \quad \sigma_\mu = 0.30\,GeV \quad \sigma_c = 0.14\,GeV \tag{9.18}$$

in Eq. 9.13 and Eq. 9.8 to obtain

$$M_{cdf1994} = 80.384 \pm 0.231\,GeV. \tag{9.19}$$

This, again, is the result obtained by CDF[39].

Combining The CDF 1991 And UA2 1992 Results: $M_{cdf,ua2}$

The masses and their errors are:

$$M_{cdf1991} = 79.91\,GeV \quad M_{ua2} = 80.37\,GeV \tag{9.20}$$

$$\sigma_{cdf1991} = 0.39\,GeV \quad \sigma_{ua21992} = 0.37\,GeV \quad \sigma_c = 0.08\,GeV \tag{9.21}$$

and the combined result:

$$M_{cdf,ua2} = 80.142 \pm 0.274\,GeV \tag{9.22}$$

The CDF 1994 And The DØ 1993 Combined Result: $M_{cdf,d0}$

We use

$$M_{cdf1994} = 80.384\,GeV \quad M_{d0} = 79.86\,GeV \tag{9.23}$$

$$\sigma_{cdf1994} = 0.231\,GeV \quad \sigma_{d0} = 0.40\,GeV \quad \sigma_c = 0.08\,GeV \tag{9.24}$$

in Eq. 9.13 and Eq. 9.8 and find:

$$M_{cdf,d0} = 80.268 \pm 0.205\,GeV \tag{9.25}$$

The World Average W Mass.

Finally, with

$$M_{cdf,ua2} = 80.142\,GeV \quad , \; M_{cdf,d0} = 80.268\,GeV \tag{9.26}$$

$$\sigma_{cdf,ua2} = 0.274\,GeV \quad \sigma_{cdf,d0} = 0.205\,GeV \quad \sigma_c = 0.08\,GeV \tag{9.27}$$

we obtain

$$\overline{M} = 80.22 \pm 0.17\,GeV \tag{9.28}$$

9.1 Constraints On Standard Model Parameters

We discussed in Chapter 2 the correlation between the top quark mass and the W mass. Fig. 9.1 shows again the correlation between the top quark mass and the W mass for different values of the Higgs mass with the constraint from the world average W mass and its error shown as a horizontal band. Electroweak radiative corrections, perturbative $\mathcal{O}(\alpha\alpha_s)$ contributions, and $t\bar{t}$ threshold effects (the Greens function approach) are incorporated[40]. Using the world average W mass, we get

$$M_{top} = 158 \pm 28^{+19}_{-15}\,GeV, \tag{9.29}$$

where the last error is due to the Higgs mass with 250 GeV as its central value, 60 GeV as the lowers limit and 1000 GeV as the upper limit.

9.2 Prospects for Improving Upon the Current Measurements

We have reported a preliminary measurement of the W mass using electrons in the central calorimeter, $|\eta| \leq 1.1$. As the analysis progresses, we expect to reduce both scale and systematic errors. We will add W and Z events with electrons detected in the end calorimeters. This will reduce the statistical error.

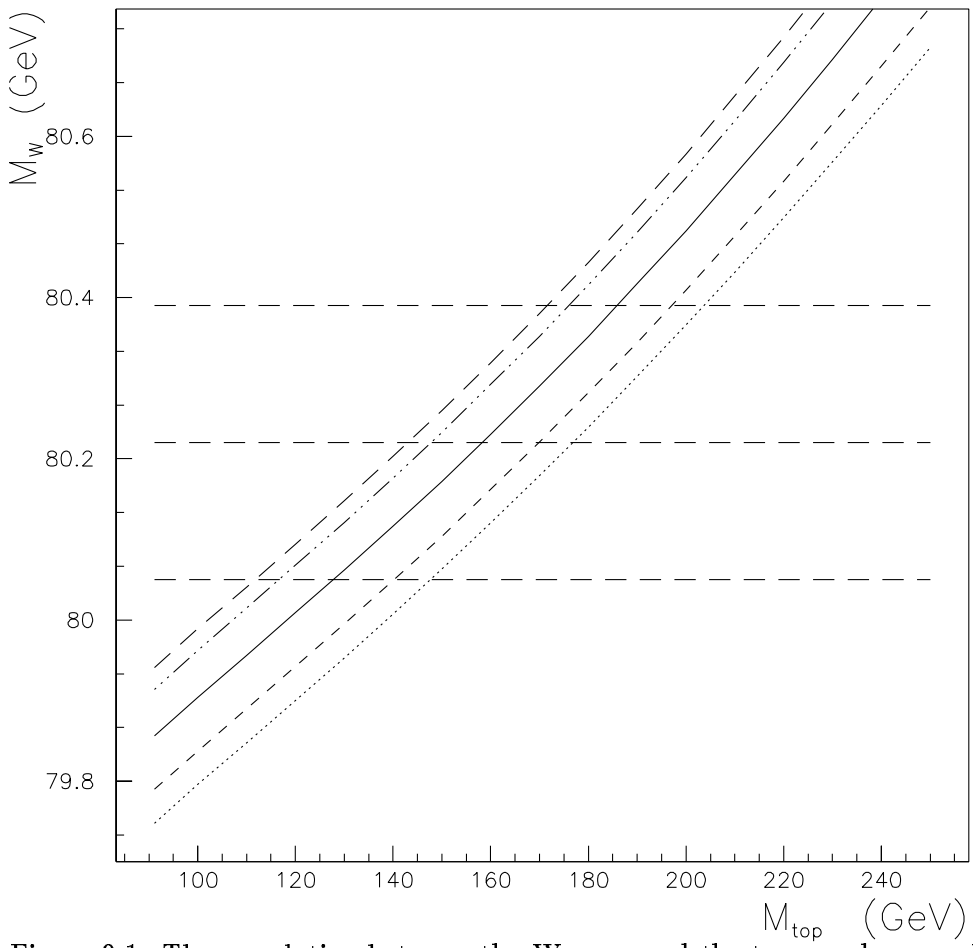

Figure 9.1: The correlation between the W mass and the top quark mass. Various curves from top to bottom correspondent to Higgs masses M_H =60, 100, 250, 600, and 1000 GeV respectively. The middle horizontal line indicates the world average value of the W mass. The upper and lower horizontal lines indicate the one sigma error on the world average.

In the current Tevatron run, Run I(b), which started toward the end of 1993, we expect to quadruple the data. Since scale and systematic errors depend primarily on the number of Z events, we shall be able to reduce the scale and systematic errors, as well as the statistical error, with the larger data sample. The statistical error will be approximately 50-80 MeV. We expect the total error to be in the range from 100 - 150 MeV. When combined with other W mass measurements, and the observation of the top quark and the measurement of its mass, this result will lead to even tighter constraints on the Standard Model.

Bibliography

[1] R. Tanaka, talk given at the XXVI Int. Conf. on High Energy Physics, Dallas, Texas, August 1992.

[2] Constraint on TOP quark mass from W mass: M. Veltman, Nucl. Phys. **B123**, 89 (1977); M. Chanowitz, M. Furman and I. Hinchliffe, Phys. Lett. **78B**, 285 (1978).

[3] E. Berger, F. Halzen, c. Kim, and S. Willenbrock, *Weak Boson Production at Fermilab Tevatron Energies*, Phys. Rev. **D40**, 83 (1989).

[4] R. Hamberg, W.L. van Neerven, *A Complete Calculation of the Order α_s^2 Correction to the Drell-Yan K-Factor*, DESY90-129.

[5] S. Weinberg, Phys. Rev. Lett. **19**, 1264 (1967).

[6] A. Salam, *Elementary Particle Physics : Relativistic Groups and Analyticity* (Nobel Symposium No. 8, edited by N. Svartholm, Almqvist and Wiksells, Stockholm, 1968) P. 367.

[7] Review articles which describe the Weinberg-Salam model in detail are E. Abers and B. Lee, Phys. Rep. **9C**, 1 (1973); M.A.B. Beg and A. Sirlin, Annu. Rev. Nucl. Sci. **24**, 379 (1974); D. Baillin, J. Phys. **G3**, 321 (1977).

[8] V. Barger and R. Phillips: *Collider Physics*, (Addison-Wesley, 1987).

[9] A. Sirlin, Radiative Corrections in $SU(2)_L \times U(1)$ Theory : A Simple Renormalization Framework, Phys. Rev. **D22**, 971 (1980).

[10] W. Marciano, *Weak mixing angle and grand unified gauge theories*, Phys. Rev. **D20**, 274 (1979).

[11] CDF Collaboration, A. Abe *et al.*, Phys. Rev. Lett. **65**, 2243 (1990).

[12] UA2 Collaboration, J. Alitti *at al.*, Phys. Lett. **B241**, 150 (1990).

[13] J. Smith, W. L. van Neerven, and J. A. M. Vermaseren, *Transverse Mass and Width of the W Boson*, ITP-SB-83-11; Phys. Rev. Lett. **50**, 1738 (1983).

[14] W. J. Marciano and Z. Parsa, Snowmass 1982, p.155.

[15] Particle Data Group, Phys. Rev. **D45**, part 2 (1992).

[16] J.F. Detoeuf *et al.*, Nucl. Instr. and Methods in Phys. Res. **A265**, 157 (1988).

[17] H. Aihara *et al.*, *Design, Construction, and Performance of the Electromagnetic Module of the DØ End Calorimeter*, Nucl. Instr. & Meth. **A 325**, 393 (1993).

[18] J. Kotcher, Ph.D thesis, *Response of the DØ Calorimeter to Cosmic Ray Muons*, Department of Physics of New York University, October, 1992.

[19] M. Narain, *Electron Identification in the DØ Detector*, Proceeding of the 7th Meeting of the American Physical Society Division of Particle and Fields, Nov. 10-14, 1992, p.1678.

[20] J. Sculli, D0 Internal Note # 937(1990).

[21] S. Feher, Proceedings of the Second International Conf. on Calorimetry in High Energy Physics, Capri Italy, Oct. 14-18 1991.

[22] M. Demarteau *et al.*, *D0 Calorimeter Electronics Performance*, Proc. of the First International Conf. on Calorimetry in High Energy Physics, Batavia, IL, Oct 29-Nov 1, 1990.

[23] Courtesy of Hiro Aihara.

[24] Geary Eppley, Private Communication. The dijet cross section from DØ data for dijets with each jet $P_T > 25$ GeV and within the fiducial regions defined by the W events is $2600 \pm 14\,nb$. This cross section is almost twice the value obtained from PYTHIA. Most of the discrepancy is in the jet rate in EC, which is not known from other experiments.

[25] J. Yu, DØ Internal Note #1685.

[26] W. Dharmaratna, DØ Internal Note #1731.

[27] P. Grannis, DØ Internal Note #796.

[28] R. Raja, 7th Topical Workshop on Proton-Antiproton Collider Physics, R. Raja, A. Tollestrup, J. Yoh eds., (World Scientific, Singapore, 1988).

[29] J.R. Incandela, *Measuring the Mass of the Z^0 in UA2*, UA2 $\overline{p}p$ Note #597.

[30] For a particle with energy E and momentum P, the rapidity of the particle is defined as $\eta^0 \equiv \ln \frac{E-P_z}{E+P_z}$. When the particle is massless or the momentum is much larger than the mass of the particle, $P \gg m$, the rapidity of the particle becomes $\eta^0 = -2 \ln \tan \frac{\theta}{2}$. So the Pseudorapidity is defined this way: $\eta = -2 \ln \tan \frac{\theta}{2}$.

[31] P. Arnold and R.P. Kauffman, *W and Z Production at Next-to-Leading Order: from Large q_T to Small*, ANL-HEP-PR-90-70.

[32] D. Anderson, Fermilab Academic Lectures Series: *Principles of EM Calorimetry*, April, 1993.

[33] T. C. Heuring, Ph.D. Thesis, DØ Internal Note #1835, p72-73.

[34] W. Dharmaratna, DØ Internal Note #1731.

[35] G. Eppley, DØ Internal Note #1856.

[36] F. Abe *et al.*, Phys. Rev. **D43**, 2070 (1991).

[37] UA2 Collaboration, Phys. Lett. **B276**, 354 (1992). In this paper, the W mass is quoted as $M_W = 80.35 \pm 0.33(stat) \pm 0.17(syst)\, GeV$. In our present table, the statistical error means the statistical error from W events. So it is 0.22 GeV in this paper. The statistical error on the Z events which is used to determined the electron energy scale is counted as a scale error in the notation of the table. The central value is re-calculated by using the W to Z mass ratio in the paper and the present LEP Z mass which is 91.187 GeV. It becomes 80.37 GeV instead of 80.35 GeV.

[38] This thesis, chapter 8.

[39] Y.K. Kim, *Electroweak Results from CDF 1992-1993 Run*, CERN seminar, March, 1994.

[40] S. Fanchiotti, B. Kniehl, and A. Sirlin, *Incorporation of QCD Effects in Basic Corrections of the Electroweak Theory*, Phys. Rev. **D48**, 301 (1993), CERN-TH-6749/92, NYU-TH-92/12/05.

[41] G. Degrassi, S. Fanchiotti, and A. Sirlin, Nucl. Phys. **B351**, 49 (1991).

[42] J. Rosner, *Electroweak Measurements and the Top Quark mass*, Rev. of Mod. Phys. **64**, 1151 (1992), also in the Proceedings of the 1992 Division of particle and Fields, Fermilab, November, 1992.

[43] L. Lyons, *Statistics for nuclear and particle physicists* (Cambridge University Press, 1989).